# Characterization of magnesium silicate hydrate (M-S-H)

Ellina Bernard, Barbara Lothenbach, Christophe Chlique, Mateusz Wyrzykowski, Alexandre Dauzères, Isabelle Pochard, Céline Cau-Dit-Coumes

# Characterization of magnesium silicate hydrate (M-S-H)

CCR

20.04.2018

Ellina Bernard[1)*], Barbara Lothenbach[1)], Christophe Chlique[2)], Mateusz Wyrzykowski[1)], Alexandre Dauzères[3)], Isabelle Pochard[4)], Céline Cau-Dit-Coumes[2)]

[1)] Empa, Laboratory for Concrete & Construction Chemistry, 8600 Dübendorf, Switzerland

[2)] CEA, DEN, DE2D, SEAD, F-30207 Bagnols-sur-Cèze cedex, France

[3)] IRSN, Institute of Radiation Protection and Nuclear Safety, PSE/SEDRE/LETIS, BP 17, 92262 Fontenay aux Roses, France

[4)] Université Bourgogne-Franche-Comté, 21078 Dijon, France

*Corresponding author: Bernard E., email: ellina.bernard@empa.ch

## Abstract (150 words max)

In this study, the structure of synthetic magnesium silicate hydrated phases (M-S-H) and the distribution of water as a function of the Mg/Si ratio were investigated. Different analytical techniques indicated that M-S-H phases are nano-crystallite hydrated phyllosilicates with relatively short coherence length (1.2 nm) and small particle size (>200 $m^2/g$). Zeta potential and cations exchange capacity measurements showed a negative surface charge on M-S-H from the deprotonation of the silanol groups. The negative surface charge is compensated by exchangeable magnesium or others cations. Combined analyses were used to characterize the water distribution in M-S-H revealing the following: i) *confined* water; its amount depends strongly on the relative humidity ii) *very confined* water (or possibly water coordinated to magnesium), and iii) hydroxyl groups bound to magnesium and to silicon.

## Keywords:

Magnesium silicate hydrate (M-S-H), structure, water content, surface properties

## 1. Introduction

Magnesium silicate hydrate (M-S-H) phases are of interest as M-S-H may form i) as a main reaction product in magnesia-silica binders which are under development as sustainable alternatives to Portland cement [1-3], ii) at the interface of cement-based materials in contact with clays [4-8] and/or iii) at the interface of cementitious materials with groundwater, seawater, and $MgSO_4$ or $MgCl_2$ solutions [9-11]. In magnesia-silica binders, magnesia and silica dissolve and react to form magnesium silicate hydrate gels. At the interface of Portland cement and blended cements, leaching and carbonation of the C-S-H decrease pH at the surface of the cement sample, resulting in the decalcification of C-S-H and the formation of amorphous silica which reacts with magnesium to form M-S-H [12, 13].

The properties and solubility of M-S-H phases synthesized in the laboratory have been studied previously [14-17]. In short term experiments (1 to 6 months), a Mg/Si of around 1.0 was reported [14, 16-21], while in long term studies (1 year or longer) [15, 22], a wider range of compositions (Mg/Si = 0.8-1.3) has been determined. For M-S-H formed at the interaction zone of cement with seawater, Mg/Si ratios up to 2 were observed for Portland cement [11] or as low as 0.5 for the interface between low-pH cement and clay rocks [5]. This wide range of compositions might be related to changes in the structure, which is investigated in the present paper.

$^{29}$Si MAS NMR studies showed that the silicates are arranged in tetrahedral layers and magnesium in octahedral layers comparable to 2:1 or 1:1 phyllosilicates as shown schematically in Figure 1. The structure of M-S-H is poorly ordered and has been related to sepiolite [14], hydrated nanoparticles of talc [16], hydrated talc or hydrated antigorite [15], lizardite [17, 23], stevensite [15] or saponite [7, 16].

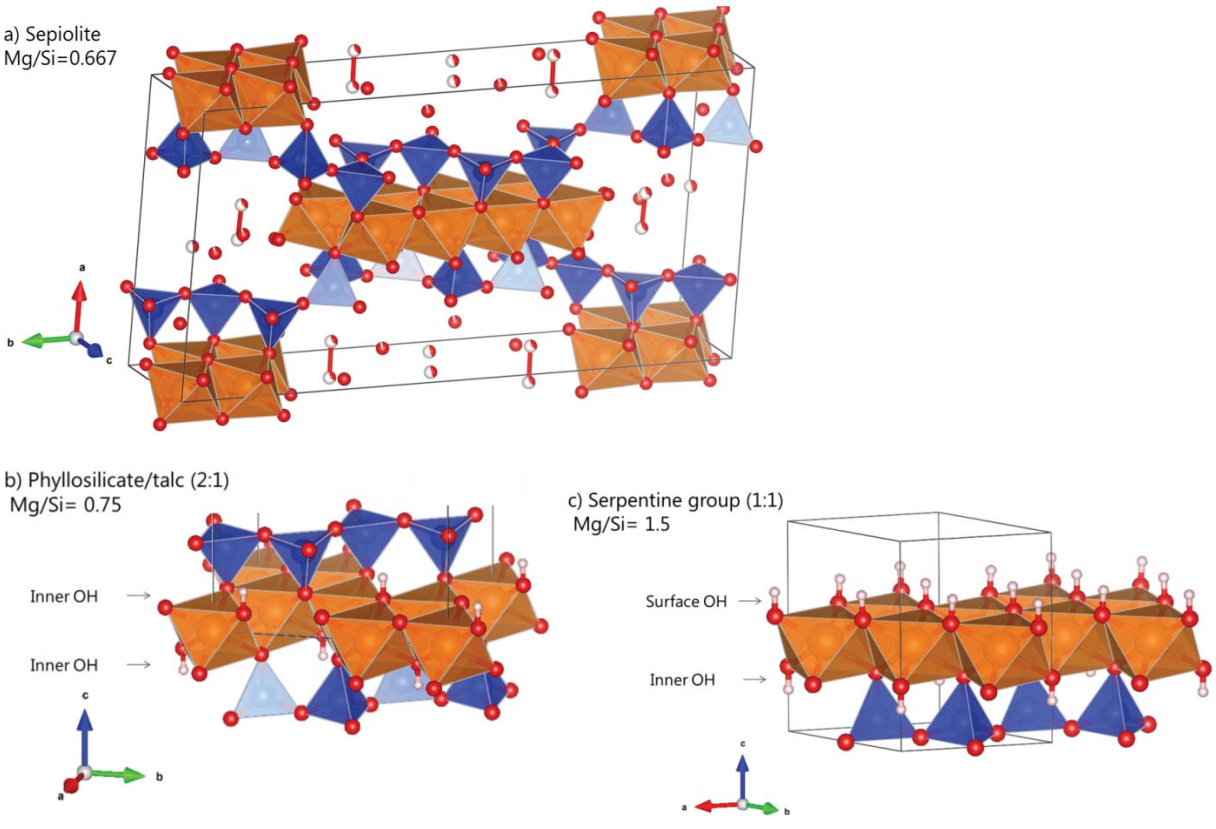

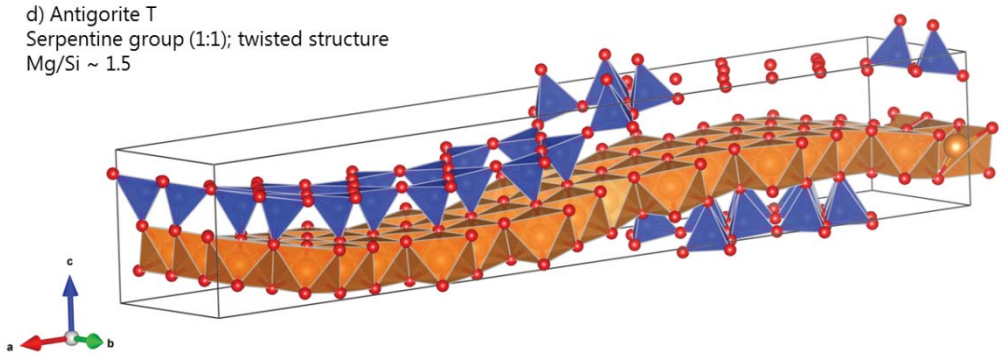


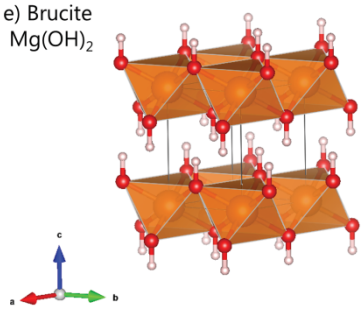


*Figure 1: Schematic sketches of the structure of a) sepiolite, T:O:T structure, b) 2:1 phyllosilicates with a T:O:T structure such as talc, c) 1:1 phyllosilicate (T:O structure) such as the serpentine group, d) brucite e) antigorite T (T:O structure phyllosilicate) (orange: octahedral magnesium site, blue: tetrahedral silicate site). The structures are from [24-28] using the VESTA software [29].*

The $^{29}$Si MAS NMR spectra of M-S-H showed approximately $^{2}/_{3}$ $Q^3$ signals indicating silica sheets and $^{1}/_{3}$ of $Q^2$ signals indicating either very small coherent areas of silica sheets and/or defects in the silicate sheets or even double chain silicate layers [15, 16]. The $Q^2$ resonance occurs at a chemical shift of -85.5 ppm, while the broad signal at -92 to -97 has been attributed to 2 or 3 different $Q^3$ silicate sites depending on the deconvolution [15, 17, 30]. Deconvolutions taking into account the presence of 3 different sites indicated chemical shifts at -92.7, -94.7 and -96.8 ppm: $Q^3_a$, $Q^3_b$, and $Q^3_c$ [15]. The "poorly-organized" character of M-S-H leads to significantly broader signals than those observed in crystalline phyllosilicates. The chemical shift at -92.7 ppm is characteristic for serpentine group minerals [15, 31] such as antigorite, chrysotile or lizardite with a T:O structure (see Figure 1), while the chemical shift of -96.8 ppm is characteristic for talc [15, 16, 32-34] with a T:O:T structure. Both classes of minerals exhibit a potentially infinite layer of silicate. The presence of a second silicate tetrahedral layer on the other side of the octahedral magnesium layer doubles the sheets of silicate (T:O:T) and results in a more negative chemical shift for silica in talc than in serpentine group minerals with a T:O structure. The intermediate $^{29}$Si MAS NMR resonance at -94.7 ppm in the M-S-H spectra could not be attributed [15, 16, 33, 34]. This intermediate chemical shift could be related i) to the presence of an empty neighboring magnesium site as in stevensite, which has as talc a T:O:T structure, but is deficient in magnesium: (□O)-Si-(O-Si)$_3$) where □ is a vacant site [32, 33], ii) to a high content of surrounding water in M-S-H structure [23], which would result in a resonance at -95 ppm as in the case of saponite, hectorite or stevensite and/or iii) to the variability of the Si-O-Si angles in M-S-H [23].

M-S-H as a precursor of sepiolite has been suggested by [14]. The $^{29}Si$ MAS NMR spectra of M-S-H shows similarities with sepiolite ($Si_6O_{15}Mg_4(OH)_2(OH_2)_2{\cdot}4H_2O$) spectrum. Sepiolite has a phyllosilicate chain-structure derived from talc T:O:T ribbons with alternate silica and magnesium layers (Figure 1a) for which, similar silicate signals as for M-S-H have been reported: one $Q^2$ (at -85.2 to -85.5 ppm) and three $Q^3$ signals (first at -92.3 to -92.7 ppm, second at -94.3 to -94.5 ppm and last at -98.2 ppm) as shown e.g. in [35]. The $Q^3_a$ signal was attributed to the near edge of the silicate sheet in the blocks while the $Q^3_b$ and $Q^3_c$ signals were attributed to the center or the edge of the silicate sheet [36-39]. Sepiolite is needle-like clay with a low charge density, low cation exchange capacity, which is not swelling. The Mg/Si ratio of sepiolite is equal to 0.667, lower than that observed in pure M-S-H [15] synthesized from MgO and silica fume, although some studies, using other raw materials, have reported such a low ratio [14, 21]. In fact, Wollast and al. [40] have observed the formation of a very poorly crystalline sepiolite-like phase from the reaction of aqueous silica with seawater comparable to M-S-H. Sepiolite contains different types of water, i) zeolitic water which can be removed by thermal treatment below 150°C, ii) coordinated water ($Mg\text{-}OH_2^+$) which is lost above 150°C and probably below 450°C and is bound to the terminal magnesium cations of the octahedral sheet and iii) structural water which corresponds to the hydroxyl group linked either to tetrahedral or octahedral layers [37, 41, 42].

Roosz et al. [16] indicated based on the X-rays diffraction (XRD) patterns of M-S-H and the presence of the $Q^2$ signal in the $^{29}Si$ MAS NMR spectra that the M-S-H had only nanometer-sized coherent scattering domains which also caused the broad reflections in the XRD pattern. The size of a coherent region of M-S-H was estimated at 1.5 nm in the ab plane, and 2.4 nm along c. Similarly, Chiang et al. [43] suggested based on SAXS measurement a spherical structure for M-S-H with an average radius of 1.7±1 nm.

In this paper, the effect of the Mg/Si ratio (ranging from 0.7 to 1.4) on the M-S-H structure, including the distribution of the water and the particle properties, were investigated by $^{29}Si$ MAS-NMR, $^{1}H\text{-}^{29}Si$ CP MAS-NMR and FT-IR spectroscopy and with X-rays diffraction and X-ray pair distribution function analysis, the water and hydroxyl contents and their distribution by DVS, TGA and $^{1}H$-NMR relaxometry, the particle size and the porosity by $N_2$ physio-sorption measurements and the surface properties by CEC and zeta potential measurements. This study aimed to contribute to a better characterization of the structure of M-S-H phases and including the different types of water in M-S-H. Two additional M-S-H samples (Mg/Si=0.8 and 1.2) were exposed to hydrothermal conditions in an autoclave (180°C for 4 days) to obtain better crystalline M-S-H phases.

## 2. Materials and methods

### 2.1. Synthesis

Magnesium oxide (Merck, pro analysis, 0.18±0.02 mass% $Na_2O$) and silica fume ($SiO_2$, Aerosil 200, 0.9 mass% HCl) were used as starting materials. Different quantities of MgO and $SiO_2$ were directly mixed with ultrapure water as detailed in [22]. The syntheses were carried out to obtain ~ 5 g of solid and a water-to-solid (W/S) ratio of 45 to ensure a homogeneous suspension and sufficient solution for analysis. All the syntheses were performed in a glovebox under a nitrogen atmosphere to minimize $CO_2$ contamination. After equilibration at 20°C during 2 or 3.3 years, the

solid and liquid phases were separated by filtration under pressure (4-5 bars $N_2$) using nylon filters (0.45 µm). Following the filtration, the solids were washed with a 50/50 (volume) water-ethanol mix and then with ethanol (94 mass % alcohol) to remove dissolved ions and to prevent the precipitation of salts during drying [44]. The samples were freeze-dried with liquid nitrogen (for approximately 20 min at -195°C) and kept at -40°C under vacuum (pressure of 0.28 mbar) for 7 days. Additional samples stopped after 3.3 years were dried in desiccators over 30% relative humidity (RH).

In addition two M-S-H (Mg/Si = 0.8 and 1.2) suspensions, which had been previously equilibrated at 20°C, were treated hydrothermally. The two suspensions were heated in a stainless steel autoclave at 180 °C for 4 days, followed by a slow cooling to room temperature during approximately 12-24 hours. The filtration process and freeze drying process was similar as described above.

The solid phases were analyzed after further equilibration in $N_2$-filled desiccators at a RH of ~ 34% (saturated $CaCl_2$ solution) for a period of 14 days or longer. After drying, the samples were gently ground by hand.

## 2.2. Analytical techniques

### 2.2.1. Ion chromatography and pH

The liquid phases were analysed by ion chromatography (IC) immediately after filtration. The dissolved concentrations of Mg, Na, K, Cl, Si in undiluted solutions or in solutions diluted by a factor 10, 100 or 1000 were quantified using a Dionex DP series ICS-3000 ion chromatography system. All concentrations were determined as duplicates and the mean value is given in the following, the measurement scatter was ≤ 10%. The pH values (±0.1) were measured at ambient temperature (23±2°C) in an aliquot of unfiltered suspension and the results were corrected to 20°C as described in [22].

### 2.2.2. Solid state NMR

The $^{29}$Si MAS NMR experiments were recorded on a Bruker Avance III NMR spectrometer using a 7 mm CP/MAS probe at 79.5 MHz applying the following parameters for the single pulse experiments: 4500 Hz sample rotation rate, minimum of 3072 scans, 30° $^{29}$Si pulse of 2.5 µs, 20 s relaxation delays, RF field strength of 33.3 kHz during SPINAL64 proton decoupling.

The $^{29}$Si NMR chemical shifts of the spectra were referenced to the most intense resonance at -2.3 ppm of an external sample of an octamethylsilsesquioxane (Aldrich No. 52,683-5) which was referenced to tetramethylsilane (TMS, $\delta^{29}$Si = 0.0 ppm). The observed $^{29}$Si resonances were analysed using the $Q^n$ classification, where a Si tetrahedron is connected to n Si tetrahedra with n varying from 0 to 4. The quantification was performed by non-linear least-square fits using the ‘‘DMFIT’’ software developed by Massiot et al.[45]. Silica fume was quantified taking into account the shift at -100.9 ppm ($Q^3$ from the surface of the amorphous silica [15, 46]) and the $Q^4$ shift at -110 ppm. However, the $T_1$ relaxation time of silica fume can be very long and the amount of silica fume generally might be underestimated. The $Q^1$ and $Q^2$ environments in M-S-H were deconvoluted using mainly Lorentzian functions while the $Q^3$ environment was deconvoluted using Gaussian functions following the procedure outlined in [22].

$^{1}H$-$^{29}Si$ cross polarization MAS NMR spectra were recorded on the same equipment applying the following parameters: 4500 Hz sample rotation rate; minimum of 1536 scans, 3 s relaxation delays, RF field strengths of 33 kHz during the polarisation transfer (ramp from 100-50%) with contact times varying from 0.5 to 5 ms using the above mentioned proton decoupling conditions.

### 2.2.3. X-ray diffraction (XRD) and X-ray pair distribution function (PDF)

XRD data were collected using a PANalytical X'Pert Pro MPD diffractometer equipped with a rotating sample stage in a □-2□ configuration applying CuKα radiation (λ=1.54 Å) at 45mV voltage and 40mA intensity with a fixed divergence slit size and an anti-scattering slit on the incident beam of 0.5° and 1°. The samples were scanned between 5° and 75° 2□ with a X'Celerator detector.

In addition to the standard XRD measurements, X-ray Pair Distribution Function (PDF) analyses were performed. This analysis focusses on the entire signals including Bragg peaks and diffuse scattering. PDF represents the distribution of interatomic distances in a compound, regardless of its crystalline state, determined experimentally by a Fourier transform of the powder pattern. PDF is thus an efficient technique for studying of short coherence lengths materials such as cements [47] or geopolymers [48]. The reduced PDF, G(r), was obtained by taking a sine Fourier transform of the measured total scattering function S(Q), as shown in equation (1), where Q is the momentum transfer given in equation (2) with θ as the scattering angle and λ as the wavelength of the incident radiation [48, 49].

$$G(r) = \frac{2}{\pi}\int_{Q_{min}}^{Q_{max}} Q[S(Q) - 1]\sin(Q_r)dQ \quad (1)$$

$$Q = \frac{4\pi sin\theta}{\lambda} \quad (2)$$

It is crucial to obtain diffraction data with a high momentum transfer (Q) in order to maximize the resolution after the Fourier transform. We therefore used an X'Celerator Panalytical diffractometer equipped with a Mo source ($\lambda_{k_\alpha} = 0.70926$Å). The powder diffraction pattern was scanned over the 6.004-153.932° angular range with a step size of 0.0083°. The total acquisition was the average of 2 runs recorded over 24 hours. The PDF and standard corrections [49] were calculated with PDFGetX2 [50]. The density number of atoms $\rho_0$ used to calculate the PDF was 0.10 atoms Å$^{-3}$. The use of a finite value of Q (17Å) for the PDF analysis led to the addition of spurious oscillations to G(r) depending on the distance r. These oscillations were smoothed by the use of a Lorch (1969) function. On the other hand, calculated PDF from ta given structure was obtained with PDFGui [51]. Due to limited Q resolution, a value of 0.05 Gaussian dampening ($Q_{damp}$) envelope was introduced in the refinement.

### 2.2.4. BET and apparent density

Nitrogen sorption isotherms were measured at 77.35 K using a Coulter SA3100 equipment. The specific surface area ($SSA_{BET}$) was obtained by using Brunauer-Emmett-Teller (BET) equation [52], in the pressure range from 0.05 to 0.2 $P/P_0$. The t-plot method [53] is used to find the non-porous surface area (so-called "external area") in the second part of the t-plot at P/P° > 0.8. The pore volume (micro and meso-pores) is then calculated by subtracting the $SSA_{t\text{-}plot}$ to the $SSA_{BET}$. The calculation of those SSA and the pore volume were made with the Beckman Coulter Sorption Analysis software. The IUPAC classification [54, 55] gave the definition: micro-pore ≤ 2 nm ≤ meso-pores ≤ 50 nm ≤ macro-pores. The measurements were performed on the samples

kept in $N_2$-desiccators equilibrated at 30% RH. Just before analysis the samples were freeze-dried for 2 hours to remove any adsorbed water molecules. The apparent density was measured by helium pycnometry with a PMI Hg-porosimeter.

### 2.2.5. FTIR

Attenuated total reflectance (ATR) Fourier Transformation-Infrared (FT-IR) spectra were recorded in the mid-region on a Bruker Tensor 27 FT-IR spectrometer between 600 and 4000 $cm^{-1}$ with a resolution of 4 $cm^{-1}$ by transmittance on small amounts of powder. The focus is made on 2600-3800 $cm^{-1}$ where the stretchings of O-H vibrations are located.

### 2.2.6. Dynamic vapour sorption (DVS) and thermogravimetric analysis (TGA)

The water adsorption and desorption isotherms were determined with a VTI-SA Dynamic Vapour Sorption Apparatus (DVS) manufactured by TA Inc. The DVS device allows continuous monitoring of the mass of the samples exposed to changing RH by means of a high-precision micro balance with an accuracy of 10 µg. The RH in the chamber was varied in the range 0-94% by a controlled flow of a mixture of dry gas ($N_2$) and wet gas (saturated $H_2O$ vapor) with accuracy ±1% as determined by a dew point analyser. The isotherms were determined at 20.0±0.1°C; as controlled by means of Peltier elements. Approximately 15 mg of 2 year-old M-S-H and 2mg of 3.3 year-old M-S-H, pre-dried in a desiccator at a 35%RH, were placed in a glass sample holder in the measuring chamber of the DVS. Changes in mass were monitored continuously and logged at 1-min intervals. Equilibrium criterion to be reached before proceeding to each next RH step was set as 0.007% of a sample mass in 5 min and the maximum length of a step was set as 12 h. At the end of the sequence of RH steps, the reference dry mass was determined by drying a sample to constant mass at 105°C and 0% RH (in DVS) and at 980 °C (in TGA). The loss of the strongly physically bound water and or very loosely bound hydroxyl groups can occur around 105°C, therefore the water content is expressed relative to the mass determined at 980 °C.

Thermogravimetric analyses (TGA) were carried out on ground powder (~30 mg) with a Mettler Toledo TGA/SDTA 8513 instrument using a heating rate of 20°C/min from 30 to 980 °C. Traces of brucite ($Mg(OH)_2$) which loses water at around 400-420°C was detected only in the samples with Mg/Si = 1.3 and 1.4.

The total water bound in M-S-H was quantified from the total water loss between 30 and 980°C and the water associated to hydroxyl groups in M-S-H was quantified from the water loss between 250 and 800°C [15]. Both results were normalized to the dry mass at 980 °C and corrected for the amount of brucite as detailed in [22]; the results are given per silica.

### 2.2.7. $^1$H NMR relaxometry

$^1$H NMR $T_2$ (spin-spin) relaxometry measurements were carried out on a Bruker Minispec NMR spectrometer operating at 7.5 MHz. The 90° pulse length was 2.9 µs. The Carr− Purcell− Meiboom−Gill (CPMG) and the quadrature echo (QE) pulse sequences were used for resolving the mobile and solid water populations, respectively. The samples previously conditioned at different RH were measured while sealed in miniature PCTFE containers, same as used in [56]. Mass measurements before and after the NMR tests were carried out to verify constant mass of the samples.

The CPMG enables probing liquid water confined in different populations (sizes) of pores owing to the property that shorter $T_2$ relaxation times correspond to stronger interactions with the solids.

This method was used for water and porosity of hydrates, e.g. calcium silicate hydrate (C-S-H) [57, 58]. Three types of water confined in microstructure have been described in C-S-H with the corresponding $T_2$: the interlayer/adsorbed water (~0.1 ms), gel water (~0.3 ms), and bulk water (comprising water in interhydrate spaces and bulk water in larger pores, 1-3 ms) [56-58]. Similarly, in swelling clays such as montmorillonite, $T_2 \leq 0.05$ ms have been assigned to hydroxyl groups in the clays, while signals at ~ 0.05-0.5 ms have been related to water in the interlayer and/or adsorbed water; the $T_2$ time varies depending on the interlayer distance. Longer relaxation times have been assigned to water present in interparticle (external) pore space [59].

The relation between the transverse relaxation time and the size of the pore can be estimated, e.g., using the fast exchange model of relaxation (3):

$$\frac{1}{T_2} \approx \frac{\lambda S}{V} \quad (3)$$

where λ is the surface relaxivity, S the surface area and V the pore volume [60].

The CPMG signal can be deconvoluted into the different exponential components using numerical inversion. Applying the ILT requires relatively high signal-to-noise ratio (S/N), usually in excess of 300-400/1; for the lower S/N the algorithm may often result in erroneous deconvoluted data with artificial peaks at low $T_2$. Typical CPMG recorded for M-S-H (Mg/Si=0.9) equilibrated at 85% RH are shown in Figure 2, and three populations of water can be found: the first at ~0.05 ms, a second at ~0.8 ms and the third above 6 ms. The structure of M-S-H and the distribution of the water in M-S-H are less known than for C-S-H or clays. Based on the assignments made for clays and C-S-H, the three different populations of water were assigned to *very confined* water (interlayer and surface), *confined* water in the micro-pores and water in the space between the M-S-H agglomerates, i.e., bulk water. The ILT was used to find the position of the $T_2$ peaks corresponding to the different populations of water. However, as long as the position of the peaks in the ILT-deconvoluted data was fairly constant between consecutive measurements, the amounts of different water populations found with the ILT were prone to a high scatter due to the aforementioned low S/N. Hence, a simple multi-exponential fitting with the constrained number and positions of the $T_2$ peaks (as revealed by the ILT) was applied here to get the repartition of the amounts of the different types of waters. The multi-exponential fitting was carried out by minimizing the sum of squared errors.

Additionally, water with shorter $T_2$ times characteristic for stronger interaction with the solids (chemically combiner water, also referred to as the *structural* or *solid* water corresponding to the hydroxyl group signal was accessed using the QE pulse sequence. The QE signals were recorded as a function of pulse gap in the range $\tau = 15-45$ μs. Those were deconvoluted into a Gaussian (structural water) and an exponential (mobile water) decay parts [57, 58].

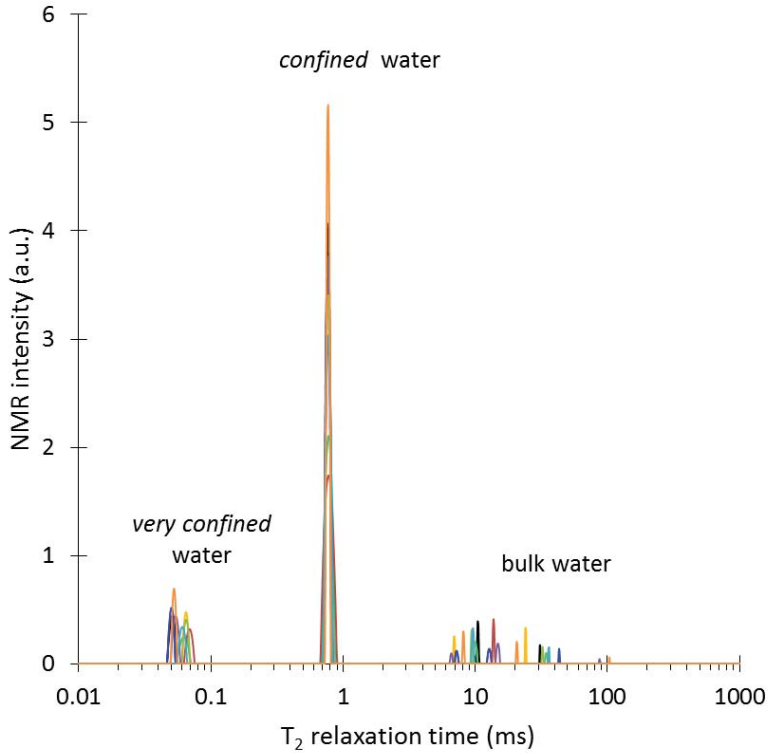


*Figure 2: 10 examples of CPMG $T_2$ results for the M-S-H 0.9 (85 %RH).*

### 2.2.8. Zeta potential measurements and cation exchange capacity (CEC)

The zeta potential was measured out directly in suspensions before filtration with 5 g of solid per 200 ml. The samples were stirred in a beaker with an overhead stirrer at 500 rpm during 10 minutes to ensure the homogeneity repartition of the particles and reach a stable value before the measurement. During the measurements, they were stirred at 400 rpm and each measurement was repeated 10 times. Zeta potential data were recorded with a ZetaProbe from Colloidal Dynamics Inc., which is based on the frequency-dependent electroacoustic effect. Shortly, an alternating voltage is applied to the suspension which causes charged particles to move back and forth at a mobility that depends on their zeta potential. The software calculates the zeta potential from the frequency-dependent mobility using the O'Brien equation [61]. Finally the values obtained were background corrected with a measurement of the filtrated aqueous phase.

Cation exchange capacity (CEC) in the samples was measured on 100 mg of powder. The cations on the surface and/or from the interlayer were exchanged with cobalt hexamine trichloride during 30 min at room temperature [4] using a solution/solid mass ratio of 30. The suspensions were filtered and the concentrations of Na, K, Ca, Mg in solution were determined by ion chromatography (IC) as detailed above. The sum of measured cations was compared to the total CEC which was obtained from the difference in the cobalt hexamine concentration from the original solution and from the leachate. Such concentrations were determined by colorimetry (absorption band at 473 nm) using a UNI-CAM UV visible spectrometer. The excellent agreement between the total CEC and the CEC calculated from the measured cations showed that dissolution of M-S-H was negligible.

# 3. Results and discussions

## 3.1. Insights on the M-S-H particles

### 3.1.1. Ageing of M-S-H

The formation of M-S-H proceeds in batch experiments very slowly such that after 1 year at room temperature thermodynamic equilibrium is generally not yet reached while after 2 years M-S-H seemed to have been near to equilibrium conditions as detailed in [22]. Thus, in addition to samples aged for 1 or 2 years [22], also well-aged samples with an equilibration time of 3.3 years were investigated. To verify that (near) equilibrium conditions have been reached, the composition of the aqueous and solid phase after 3.3 years were compared to M-S-H equilibrated for 1 and 2 years and to M-S-H which has been prepared at 180°C (hydrothermally prepared: "M-S-H HT"). Dissolved concentration and pH values measured in the aged samples (3.3 years) are presented in Table 1. The concentrations and pH measured after 3.3 years were comparable to the 2-year old samples which indicated that 3.3 years samples, as well as the 2 years ones, were close to thermodynamic equilibrium.

*Table 1: Measured dissolved concentrations in the solutions and measured pH values in equilibrium with the synthesized M-S-H samples after 1, 2 [22] and 3.3 years of curing at 20°C and with the hydrothermally prepared M-S-H (0.8 and 1.2).*

| | mmol /L | Mg | Si | Na | pH (20°C) |
|---|---|---|---|---|---|
| room temperature | | | | | |
| 1 year | 0.8 | 0.33 | 1.36 | 0.33 | 8.5 |
| | 0.9 | 0.32 | 0.66 | 0.38 | 8.7 |
| | 1.0 | 0.26 | 0.07 | 0.41 | 9.3 |
| | 1.1 | 0.13 | 0.02 | 0.43 | 9.9 |
| | 1.2 | 0.10 | 0.004 | 0.44 | 10.3 |
| | 1.3 | 0.10 | 0.003 | 0.47 | 10.4 |
| | 1.4 | 0.13 | 0.004 | 0.49 | 10.4 |
| 2 years | 0.7 | 0.37 | 1.47 | 0.34 | 8.2 |
| | 0.8 | 0.38 | 1.44 | 0.38 | 8.3 |
| | 0.9 | 0.40 | 0.34 | 0.42 | 8.6 |
| | 1.0 | 0.35 | 0.06 | 0.46 | 9.2 |
| | 1.1 | 0.15 | 0.008 | 0.45 | 9.8 |
| | 1.2 | 0.13 | 0.008 | 0.48 | 10.0 |
| | 1.3 | 0.09 | 0.003 | 0.50 | 10.3 |
| | 1.4 | 0.12 | 0.001 | 0.51 | 10.3 |
| 3.3 years | 0.7 | 0.39 | 1.49 | 0.34 | 8.3 |
| | 0.8 | 0.38 | 1.26 | 0.37 | 8.3 |
| | 0.9 | 0.41 | 0.46 | 0.42 | 8.5 |
| | 1.0 | 0.43 | 0.05 | 0.45 | 9.1 |
| | 1.1 | 0.25 | 0.009 | 0.47 | 9.7 |
| | 1.2 | 0.23 | 0.005 | 0.51 | 9.9 |

| | | | | | |
|---|---|---|---|---|---|
| | 1.3 | 0.18 | <0.002 | 0.52 | 10.3 |
| | 1.4 | 0.15 | <0.002 | 0.53 | 10.4 |
| M-S-H HT | | | | | |
| | 0.8 | 0.24 | 1.821 | 0.38 | 8.1 |
| | 1.2 | 0.35 | 0.024 | 0.53 | 9.2 |

321

322 Also, the $^{29}$Si MAS NMR spectra of M-S-H samples cured 3.3 years at room temperature were
323 compared to the spectra of the 1 year-old samples and to the hydrothermally prepared M-S-H in
324 Figure 3. The overall shapes of the spectra were similar between the 1 year and 3.3 years
325 samples.

326 The deconvolutions of the spectra are detailed in Table 2. The M-S-H 0.8 aged for 3.3 years
327 showed a lower content of $Q^2$ and higher content of $Q^3_{tot}$ resulting in a reduced $Q^2/Q^3$ than the
328 sample aged for 1 year. This more significant degree of polymerization in the old sample
329 indicates that with time the structure of low Mg/Si M-S-H becomes more similar to talc, which
330 shows a single, rather narrow $Q^3$ band at -97 ppm [32-34]. Also the hydrothermally prepared M-
331 S-H showed a higher degree of ordering and a more distinct but still rather broad band -96.5 ppm.
332 This trend of higher ordering at higher temperature agrees with other findings [62, 63], who
333 observed a progressive better ordered structure for M-S-H formed at higher temperatures and the
334 formation of talc at 600°C.

335 For the M-S-H 1.2 sample which contains more magnesium, the amount of $Q^1$, $Q^2$ and $Q^3_{tot}$ did
336 not change significantly between 1 to 3.3 years. However, a higher intensity of the signal at -92.7
337 ppm ($Q^3_a$) after 3.3 years indicated a somewhat greater degree of organization and a structure
338 related to serpentine group minerals such as lizardite or antigorite (Mg/Si=1.5, T:O structure, see
339 Figure 1). The hydrothermally prepared M-S-H 1.2 showed one only $Q^3$ band at -93 ppm which
340 would be consistent with a 1:1 T:O well-ordered structure.

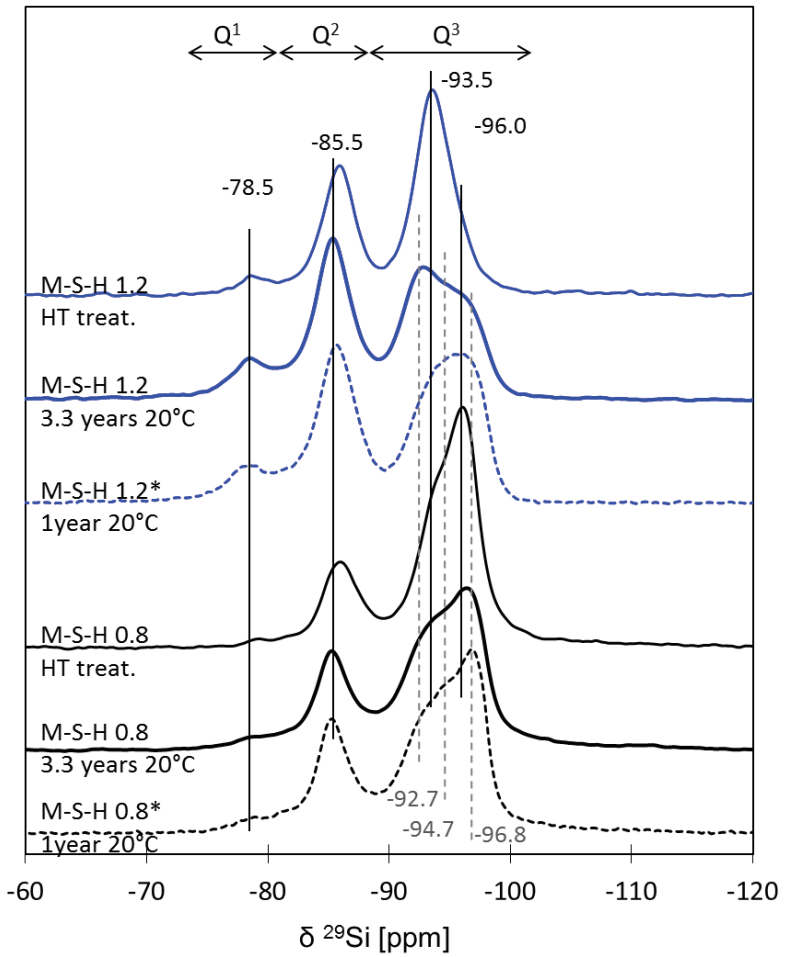


*Figure 3: $^{29}$Si MAS NMR spectra of the M-S-H hydrothermally prepared (0.8 and 1.2) compared to $^{29}$Si MAS NMR spectra of M-S-H samples synthesized at 20°C after 1 year (*=from[22]) or 3.3 years of curing.*

*Table 2: Chemical shifts and relative intensities of different silicon sites obtained from the deconvolution of the $^{29}$Si MAS NMR spectra of M-S-H synthesized at room temperature and prepared hydrothermally (HT) presented in Figure 3.*

| | | M-S-H (room temperature) | | | | | |
|---|---|---|---|---|---|---|---|
| | | $Q^1$ -78.3 ±0.3 ppm | $Q^2$ -85.5 ±0.3 ppm | $Q^3_a$ -92.7 ±0.3 ppm | $Q^3_b$ -94.7 ±0.3 ppm | $Q^3_c$ -96.7 ±0.3 ppm | $Q^2/Q^3$ |
| 0.8 | 1 year | 3 | 34 | 25 | 8 | 26 | 0.6 |
| 0.8 | 3.3 years | 2 | 28 | 26 | 17 | 23 | 0.4 |
| 1.2 | 1 year | 7 | 46 | 14 | 12 | 21 | 1.0 |
| 1.2 | 3.3 years | 8 | 47 | 25 | 6 | 14 | 1.0 |

| | | M-S-H (HT. prepared) | | | | | |
|---|---|---|---|---|---|---|---|
| | | $Q^1$ -79.0 ±0.5 ppm | $Q^2$ -85.8 ±0.5 ppm | $Q^3_a$ -93.7 ±0.5 ppm | | $Q^3_c$ -96.2 ±0.5 ppm | $Q^2/Q^3$ |

| | | | | | | |
|---|---|---|---|---|---|---|
| 0.8 | HT | 0 | 22 | 30 | 48 | 0.3 |
| 1.2 | HT | 5 | 32 | 63 | 0 | 0.5 |

*Quantification error ≃ ± 10% of absolute amount of (%Si) +2.5%.*

In summary, M-S-H synthesized at room temperature were similar after 1 or 3.3 years although the longer reaction time resulted in slightly better-ordered structures. The M-S-H 0.8 HT structure is comparable to a poorly ordered 2:1 phyllosilicate such as talc or stevensite while M-S-H with a higher Mg/Si showed instead a structure similar to a 1:1 phyllosilicate such as antigorite. In all cases, a significant amount of $Q^2$ was still present, also in the hydrothermally prepared samples.

### 3.1.2. X-rays diffraction

#### *3.1.2.1. X-ray diffraction patterns*

The XRD patterns of the M-S-H phases with different Mg/Si ratios together with the hydrothermally prepared M-S-H are shown in Figure 4a. XRD patterns showed very broad reflections. The patterns were very similar with equal relative intensity and positions of the broad reflections independent of the Mg/Si ratio. The humps have been indexed, in Figure 4a, following the indexing of M-S-H based of talc, $Mg_3Si_4O_{10}(OH)_2$, from [16] and also based on the structure of kerolite, $Mg_3Si_4O_{10}(OH)_2.H_2O$, a hydrated variety of talc from [64, 65] and of deweylite from [66], a naturally occurring hydrous amorphous magnesium silicate with a composition between $Mg_3Si_4O_{10}(OH)_2$ 0.3-0.7$H_2O$ and $Mg_3Si_2O_5(OH)_4$0.3-0.7$H_2O$. Kerolite or deweylite had been described by [64-66] as extremely fine-grained or disordered talc or stevensite minerals possibly mixed with minerals from the serpentine group such as lizardite or antigorite. Similar to the reflection profiles of M-S-H, the XRD patterns of these materials are broad indicating extremely small crystallite size, disorder or both. Lin et al. [67] compared M-S-H-like phase to hectorite, swelling clay, and indexed the broads reflections as detailed in Figure 4b.

The reflections at 59.9 °2θ are shifted to slightly lower angles at higher Mg/Si (both for preparations at ambient and hydrothermal temperatures). These reflections are characteristic for the main layer of trioctahedral phyllosilicates. This difference from M-S-H 0.8 to M-S-H 1.2 is consistent with the slight increase of the 060 distance from 1.528 Å (60.5 °2θ) in 2:1 phyllosilicates (talc) to 1.54 Å (60.05 °2θ) in 1:1 phyllosilicates (serpentine). This indicates only small changes in the large scale of the sheets arrangement.

The reflection at 27.2°2θ corresponds to the (003) distance of talc and is better defined in the M-S-H 0.8HT sample. A reflection at 24.9°2θ can be observed in M-S-H 1.2HT, which could be attributed to the (002) of the serpentine mineral. Those observations confirmed a high resemblance of the hydrothermally prepared M-S-H with the two end-members talc (2:1) in the case of M-S-H 0.8HT and serpentine (1:1) minerals in the case of M-S-H 1.2HT.

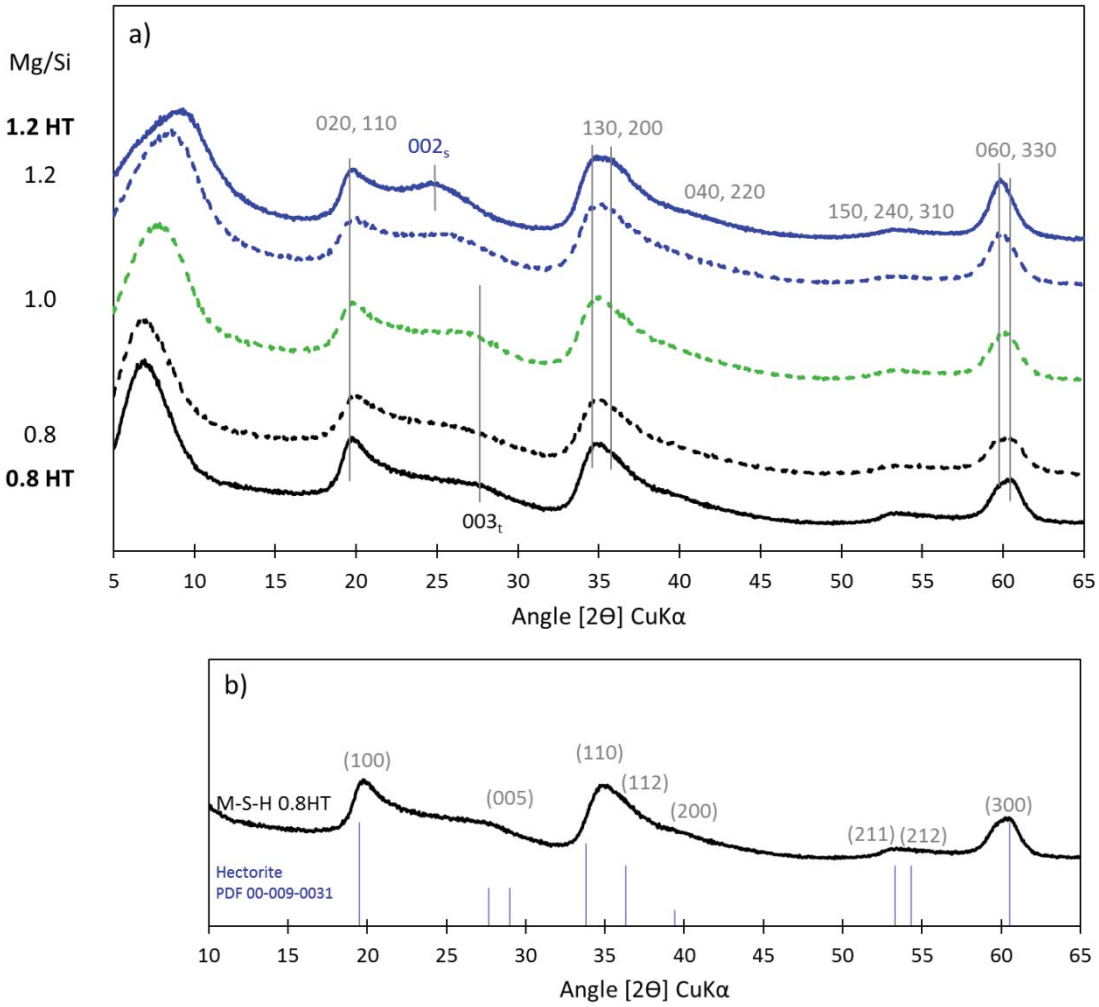


*Figure 4: a) XRD patterns of M-S-H samples (3.3 years, 20°C) and of hydrothermally treated M-S-H indexed following kerolite, $Mg_3Si_4O_{10}(OH)_2.H_2O$ (0.8: $(003)_t$ for talc and 1.2$(002)_s$ for serpentine); b) XRD patterns of M-S-H 0.8 HT indexed following hectorite.*

### *3.1.2.2. Basal spacing drying and swelling*

The main difference between the patterns of M-S-H (Figure 4) was in the reflection at 7-9 °2θ which corresponds to layer-to-layer (001) distance as detailed in [16]. As discussed in [16], the minimal coherent regions in M-S-H phases can lead to shifts of the signals related to the 001 distance which can result in an overestimation of this distance. The 001 distance of the M-S-H 0.8 was at the detection limit and could be larger than the 12.7 Å indicated in Figure 5. The measured layer-to-layer distances of the M-S-H synthetized at room temperature and hydrothermally prepared are plotted in Figure 5 as a function of the Mg/Si.

An increase of Mg/Si ratio from 0.8 to 1.2 resulted in a shift of the first reflection from 7.0 to 8.6° 2θ indicating a decrease of the mean basal spacing from at least 12.7 Å to 10.3 Å.

The drying procedure affected the measured (001) distance, as visible at high Mg/Si. The freeze dried samples re-equilibrated to 33 % RH always showed a lower layer-to-layer distance than samples which were dried directly to 33 % RH, without initial freeze drying as shown in Figure 5, indicating that freeze drying resulted in a collapse of the interlayer which was not or only partially restored during rehydration.

The addition of ethylene glycol to the freeze-dried samples resulted in an increase of their layer-to-layer distances indicating a swelling of the M-S-H as also characteristic for hydrated 2:1 phyllosilicates with layer charge. At low Mg/Si, the (001) the distance was either too big to be measured (>12.7) or non-existing while at high Mg/Si the distance increased 10.3 to 11.6 Å.

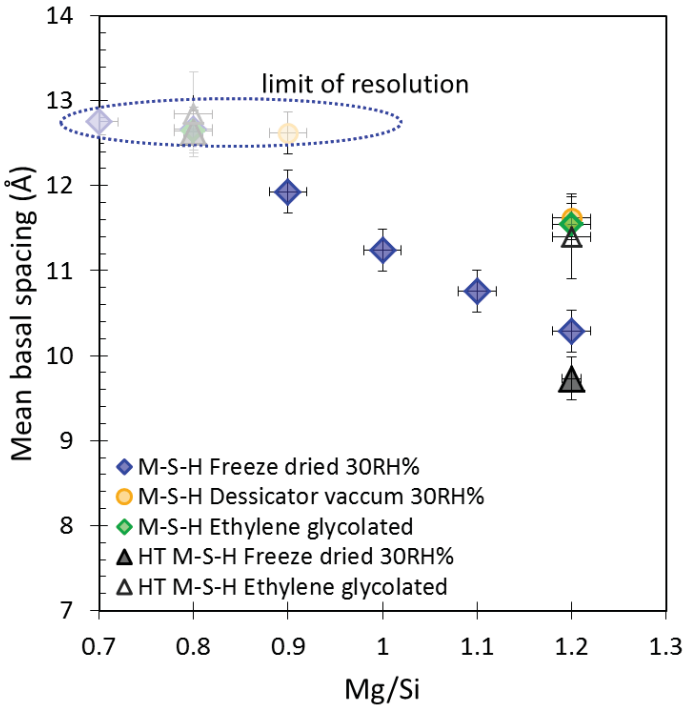


*Figure 5: Mean basal spacing (layer-to-layer distance) measured from XRD patterns of the M-S-H samples (diamonds and circles) and for hydrothermally prepared M-S-H (triangles) as a function of Mg/Si in M-S-H. Freeze dried = freeze dried samples and re-equilibrated to 33RH% over $CaCl_2$, desiccator vacuum= directly dried over $CaCl_2$ 33RH% (*might be not completely equilibrated) in a vacuumed desiccator.*

### *3.1.2.3. X-ray pair distribution function (PDF)*

Additional characterizations of the M-S-H samples were performed using X-ray pair distribution function (PDF) analysis (Figure 6). The X-ray PDF analyses of the M-S-H samples were very similar regardless the Mg/Si ratio (Figure 6a). Figure 6b compares the pair distribution functions of M-S-H, sepiolite [24], talc [25], antigorite T [28] and brucite [26]. The structures of these minerals are schematically represented in Figure 1. Antigorite (Figure 1d) corresponds to a 1:1 phyllosilicate (serpentine group) and differs from lizardite (Figure 1c) by a curved structure with alternated T:O blocks.

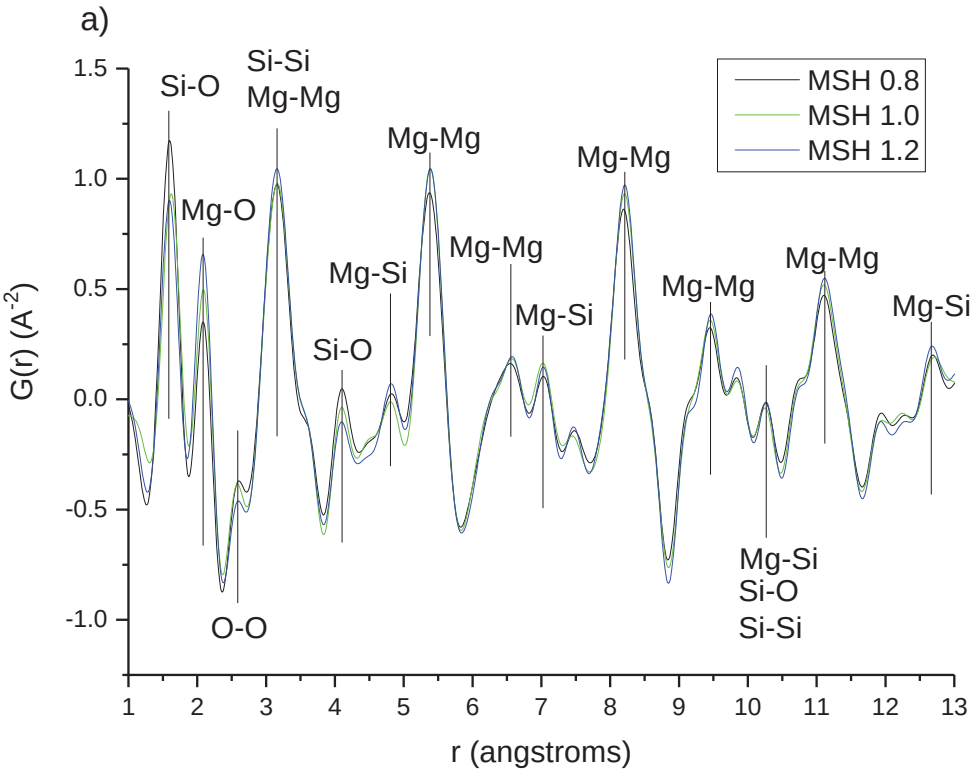
a)
MSH 0.8
MSH 1.0
MSH 1.2
Si-O
Si-Si
Mg-Mg
Mg-O
Mg-Mg
Mg-Mg
Mg-Mg
Mg-Si
Mg-Mg
Mg-Si
Mg-Mg
Si-O
Mg-Si
Si-O
Si-Si
O-O
G(r) (A-2)
r (angstroms)

419
420

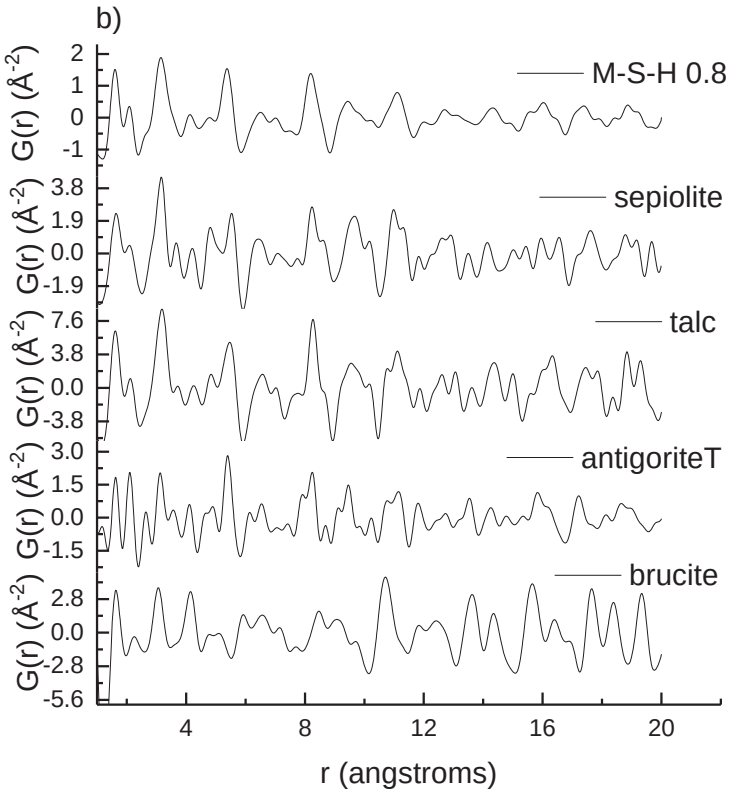
b)
M-S-H 0.8
sepiolite
talc
antigoriteT
brucite
G(r) (Å-2)
r (angstroms)

421

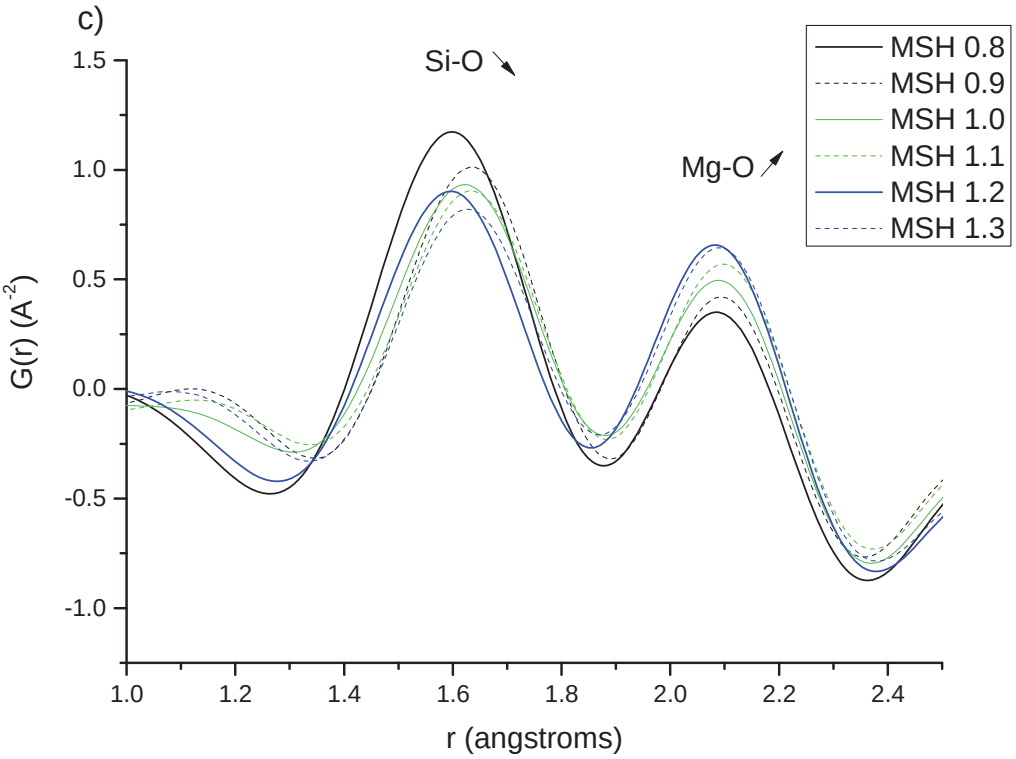


*Figure 6: a) X-ray pair distribution function of M-S-H 0.8, 1.0 and 1.2, b) 2X-ray pair distribution function of M-S-H 0.8 compared to X-ray pair distribution functions of sepiolite, talc, antigorite T and brucite, c) Zoom on X-ray pair distribution functions of M-S-H 0.8 to 1.3.*

Compared to the crystalline minerals which showed a coherence length higher than 20 Å (Figure 6b), M-S-H exhibited a rather short coherence length, close to 12 Å (Figure 6b) whatever the Mg/Si ratio, which is consistent with their poorly crystalline nature and the nano-sized particles [16, 43] as previously discussed.

The peaks were tentatively assigned using the structures of talc and antigorite as references [25, 28]: they mainly corresponded to Mg-Mg (r = 3.13 Å, 5.36 Å, 8.21 Å, 9.42 Å, 11.06 Å) and Mg-O (2.09 Å) distances within the same layer as well as Si-Si (3.20 Å) and Si-O distances in tetrahedral silicate layer (r =1.61 Å). The X-ray PDF analysis of M-S-H confirmed a structure where magnesium is bound to oxygen in the surrounding of silicon and hydroxyl groups. The intensity of the Si-O peak at r = 1.6 Å decreased whereas that of the Mg-O peak at r = 2.1 Å increased at high Mg/Si ratio, which was consistent with the depletion of $SiO_2$ and the enrichment in MgO (Figure 6c). The slight variations in the positions of the peak maxima were due to experimental uncertainties.

In a second stage we tried to fit the pair distribution functions of M-S-H by refining the structures of the different phyllosilicate minerals using the PDFgui software [51]. The refined parameters included the scale factor, the lattice parameters (a, b and c, the angles being kept constant), the isotropic displacement parameters of Mg, Si and O, and $\delta_1$, a coefficient for (1/r) contribution to the peak sharpening (for small distances, the motion of two contributing atoms can be correlated). The instrumental resolution parameter was determined by refinement of a nickel reference sample as $Q_{damp}$ = 0.05. The calculations were performed over the 1-20 Å range. Figure 7

compares the pdf function of M-S-H 1.3 with those resulting from the refinement of sepiolite [24], talc [25], chrysotile [68], lizardite [27], antigorite M (monoclinic) and antigorite T (triclinic) [28]. The fit parameters are detailed in the Appendix. The best fit, corresponding to the lowest residuum $r_w$ (quality weighted parameter characterizing the difference between observed and simulated pdfs) was obtained for triclinic antigorite Tb [28]. Antigorite has an alternating-curved structure slightly deficient in magnesium and hydroxyl groups. Antigorite Tb, described by [28], shows one or more offsets in the octahedral sheet at the change of T:O. At this offset, the coordination number of the magnesium atoms decreases and oxygen atoms in the vicinity form a tetragonal pyramid around it. Chrysotile was the second best fit. This mineral is composed of tubular fibers due to the rolls up of the sheets. The pdf results are consistent with the $^{29}$Si MAS NMR data showing a silicate structure of M-S-H 1.3 similar to that of the phyllosilicates of the serpentine group. The better fits with chrysotile and antigorite T rather than with lizardite and antigorite M would indicate that the stacking of sheets is wavy and the T:O-like blocs are randomly repeated. The chemical composition and the nano-crystallinity of the M-S-H 1.3 sample would suggest a structure close to that of antigorite rather than chrysotile which has the almost ideal chemical composition $Mg_3Si_2O_5(OH)_4$ (Mg/Si = 1.5), causing the fibrous shape (as the octahedral sheet is larger than the tetrahedral sheet).

Similarly, the X-ray pair distribution function of M-S-H 0.8 was fitted by refining the structures of lizardite, chrysotile, antigorite (monoclinic or triclinic) talc and sepiolite as shown in Figure 8. The best fit was surprisingly achieved with triclinic antigorite Tb, followed by talc and sepiolite. A structure close to that of triclinic antigorite, as for M-S-H 1.3, would be consistent with the fact that these two samples exhibit similar XRD patterns and pair distribution functions. It would also suggest a wavy structure at low Mg/Si ratio. However, the results obtained by other characterization techniques rather indicate a talc-like structure: the Mg/Si ratio of M-S-H 0.8 is close to that of a 2:1 phyllosilicate; M-S-H 0.8 HT and talc exhibit strong resemblance, as shown by X-ray diffraction and $^{29}$Si MAS-NMR.
Looking more closely at the fit obtained with the refined structure of talc, it can be seen that the quality of the fit decreased for r distances above the coherence length of the M-S-H particles (12 Å). Restricting the fit calculations to the 1-12 Å range provided vey good results (Figure 9), both with talc and antigorite ($r_w$ = 0.42 in both cases). Complementary techniques and/or a better resolution (provided by a high energy synchrotron source) are thus necessary to discriminate between the two structures.

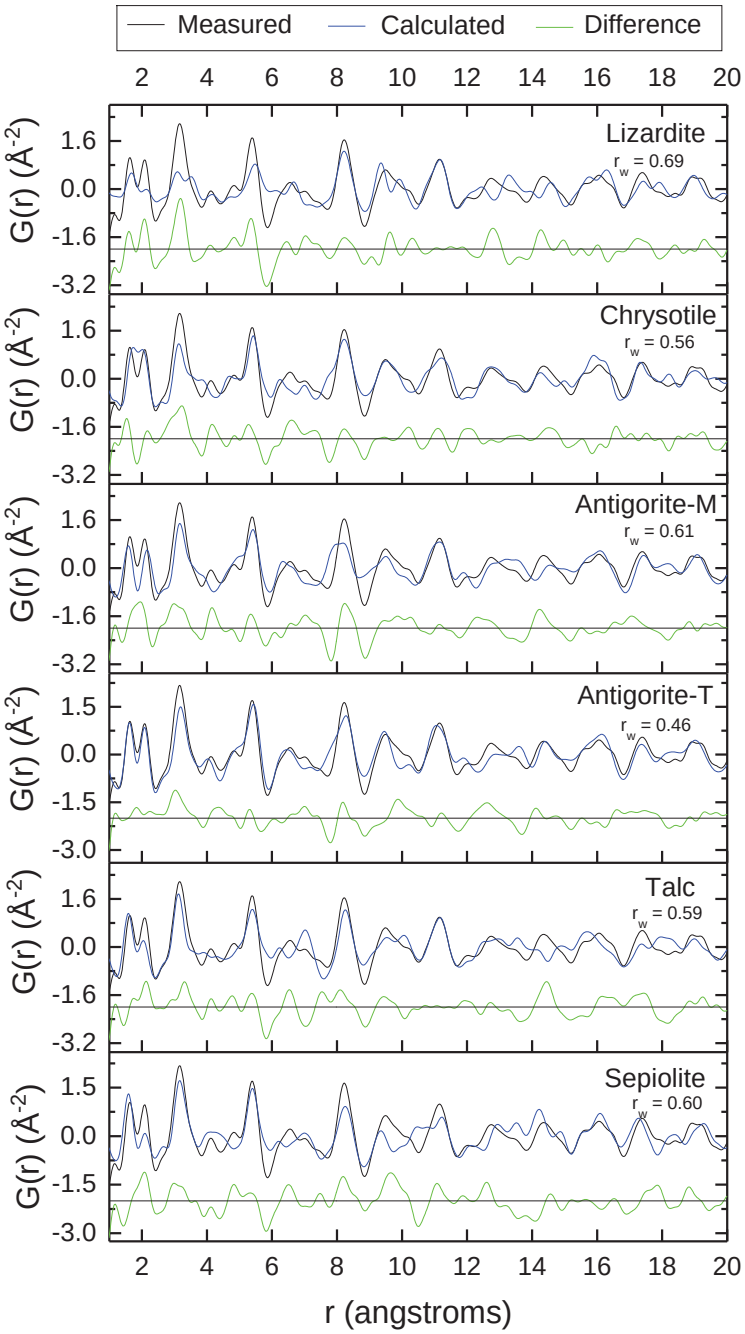


*Figure 7: Comparison of M-S-H 1.3 X-ray distribution function with those of the refined structures of lizardite, chrysotile, antigorite, talc and sepiolite over the range 1-20 Å (details of the fits in the Appendix).*

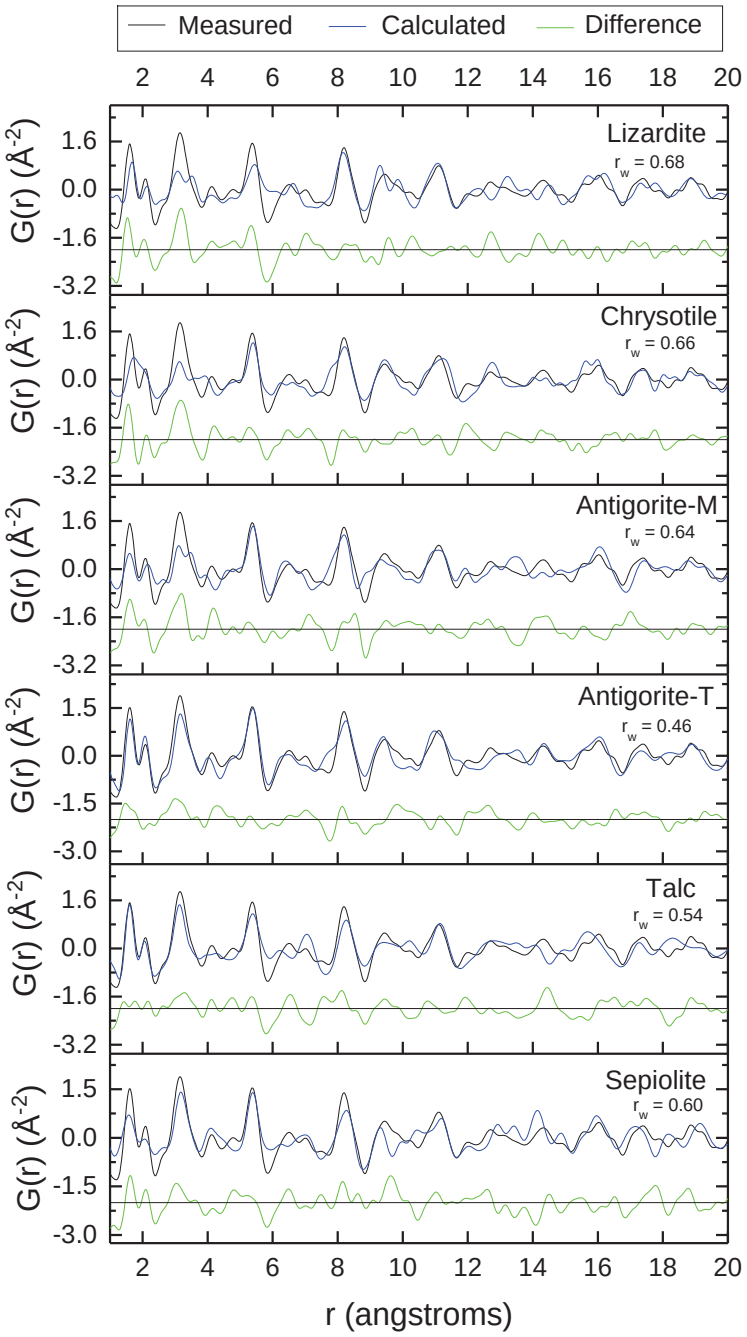


*Figure 8: Comparison of M-S-H 0.8 X-ray distribution function with those of the refined structures of lizardite, chrysotile, antigorite, talc and sepiolite over the range 1-20 Å (details of the fits in the Appendix).*

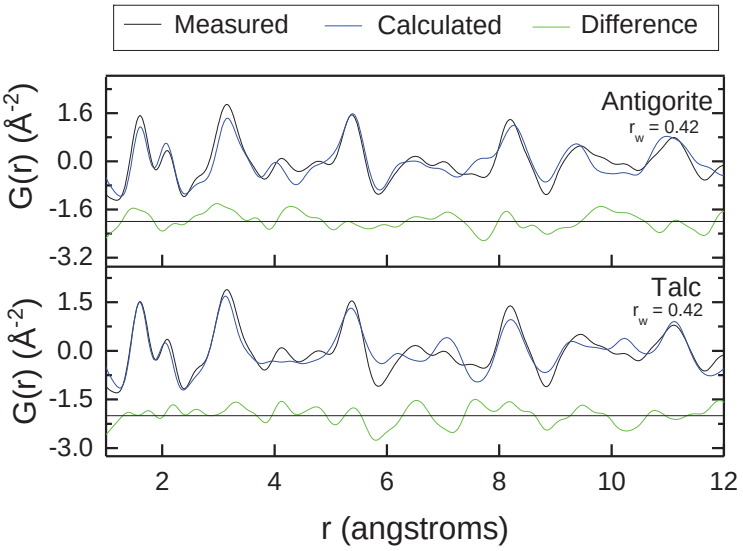


*Figure 9: Comparison of M-S-H 0.8 X-ray distribution function with those of the refined structure of triclinic antigorite (Tb) and talc over the range 1-12 Å (details of the fits in the Appendix A).*

The X-ray PDF analyses of M-S-H showed similar atoms distances in M-S-H as in phyllosilicate minerals and thus agree with the $^{29}$Si MAS NMR data: M-S-H phases are composed of silicate sheets with small coherent regions.

### 3.1.3. Particle size, porosity, and density

M-S-H samples of 3.3 years were characterized by $N_2$ physio-sorption measurements. The isotherms with the presence of hysteresis loops (Figure 10) were of the IV type according to the IUPAC classification [54]. The initial vertical slope is characteristic of the presence of microporosity (equivalent diameter between 0.4 nm and 2 nm). The adsorption part of the Type IV isotherm can be attributed to monolayer-multilayer adsorption. The hysteresis had been associated to capillary condensation taking place in meso-pores (diameter between 2 nm and 50 nm). The general features of the $N_2$-isotherm were similar to those observed for phyllosilicates synthesized at room temperature such as reported for synthetic clay-like hydrated hetorite, stevensite or saponite [33, 69, 70] or talc [71].

The M-S-H samples synthesized at room temperature exhibited an H2 or H4 hysteresis characteristic of plate-like materials with meso-pores [54]. The H2 hysteresis is characteristic of less ordered material than H4. The micro-porosity (< 2 nm) in clay usually corresponds to the interlayer, and the meso-porosity corresponds to meso-pores formed between the particles (particularly during acid treatment) [72].

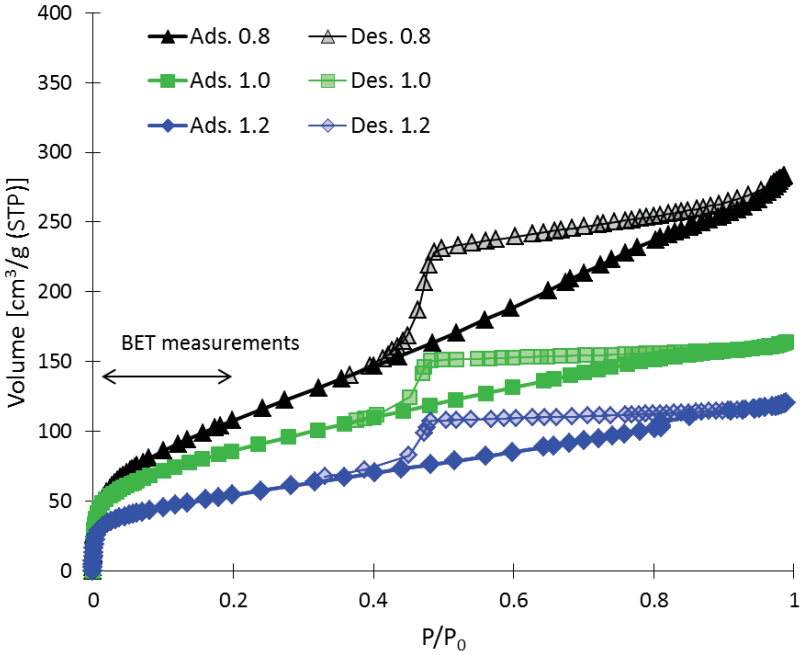


*Figure 10: $N_2$ adsorption-desorption isotherms of the M-S-H samples 0.8, 1.0 and 1.2 (synthetized at room temperature during 3.3 years).*

The specific surface areas ($SSA_{BET}$) were calculated from the $N_2$ physio-sorption measurements by applying the BET equation in the P/P° range 0.05 to 0.2 [52]. An $SSA_{BET}$ of 406, 315 and 194 $m^2/g$, respectively, was calculated for M-S-H 0.8, 1.0 and 1.2 after 3.3 years (Figure 11). The relatively high measured $SSA_{BET}$ for M-S-H were similar to the large surface area reported for synthetic clayey materials [33, 69, 70], where macro and mesopores are present together with micro-pores, while the SSA of talc has been measured to be 20 $m^2/g$ [71]. The $SSA_{BET}$ of synthetic clay has been observed to increase with the water to solid ratio used during the synthesis [70]. Thus, M-S-H formed in non-diluted systems or in field experiments might exhibit a smaller SSA.

Figure 11 shows the $SSA_{BET}$ as a function of the Mg/Si in M-S-H and at different curing times and temperatures. The $SSA_{BET}$ decreased with the Mg/Si in M-S-H. The curing temperature, 20 or 50°C, did not influence the $SSA_{BET}$. The $SSA_{BET}$ was lower for the older samples indicating the formation of slightly bigger particles with time. The $SSA_{BET}$ for M-S-H 0.8 (~ 400 $m^2/g$) was 2 times higher than for M-S-H 1.2 (~ 200 $m^2/g$).

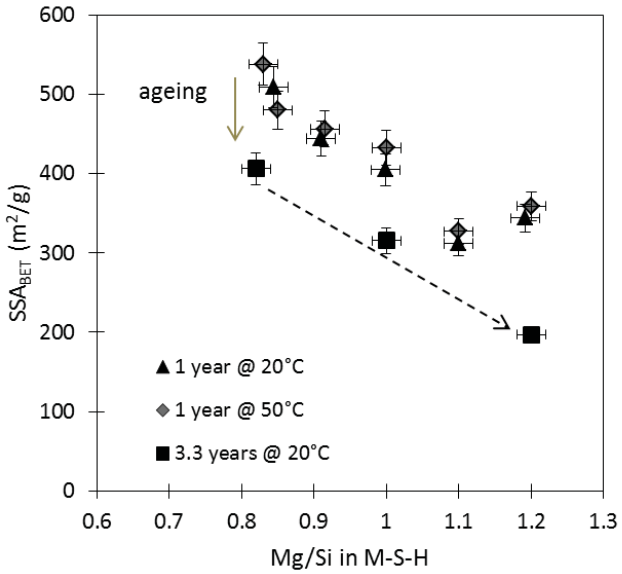


*Figure 11: Specific surface area ($SSA_{BET}$) found in M-S-H as a function of the Mg/Si in M-S-H and of the curing time.*

The t-plot method (detailed in section 2.2.4) quantifies the external surface *i.e.*, the surface without the micro/meso-porosity. The external surface variations follow the $SSA_{BET}$ with a decrease with the increase in Mg/Si ratio, but much lower values (*e.g.*, 80 m²/g for the external surface compared to 400 m²/g for the $SSA_{BET}$ for M-S-H 0.8). This denotes a high micro/meso-porosity in these samples as illustrated by the values of the pore volume in Table 3 (up to 0.113 $cm^3/g$ for M-S-H 0.8). However, this volume decreased with the increase of the Mg/Si in M-S-H and the reduction of the specific surface area. The grain density of M-S-H measured by helium pycnometry was relatively constant between 2 and 2.1 $g/cm^3$ (Table 3) in M-S-H independently of the Mg/Si.

*Table 3: Specific surface area (SSA) for M-S-H equilibrated for 3 years and hydrothermally prepared (HT) calculated by BET and t-plot methods from nitrogen isotherms and grain density (which has been measured on 3 months and 6 months samples).*

| | **BET** | | t-plot | | | |
|---|---|---|---|---|---|---|
| | **SSA[a]** | C value[b] | SSA[c] (external surface) | Vads[d] | Pore volume[e] | Grain density[f] |
| | **$m^2/g$** | | $m^2/g$ | $cm^3/g$ STP | $cm^3/g$ STP | |
| 0.8 | **406** | 46 | 80 | 73 | 0.113 | 2.1 |
| 1.0 | **315** | 74 | 21 | 68 | 0.105 | 2.0 |
| 1.2 | **194** | 112 | 17 | 41 | 0.063 | 2.1 |
| 0.8HT | **378** | 62 | | | | |
| 1.2HT | **340** | 105 | | | | |

[a] *Calculated with the BET equation for 0.05 < P/P° < 0.2*
[b] *BET C constant value*
[c] *external surface calculated according to the t-plot method [52]*
[d] *the volume adsorbed in the micro and meso pores*
[e] *Vads/647 (gas/liquid volume ratio ~ 647 for $N_2$ at 77 K)*
[f] *averaged values of the measurements on the samples synthetized 1 year at 20°C and 3 months at 50°C (standard deviation ± 0.05).*

548 $N_2$ physio-sorption measurements on the hydrothermally treated M-S-H indicated also type IV
549 isotherms according to the IUPAC classification, but an H3 hysteresis (Figure 31). The H3
550 hysteresis is related to aggregated materials with plate-like structure creating slit-shaped pores.
551 This confirms a better organization of the structure of the hydrothermal treatment of the M-S-H
552 and indicates the presence of a second porosity, which may be due to different packing. In these
553 two cases, the conditions were not recovered to apply the t-plot method for the calculation of the
554 external surface (probably due to the capillary condensation in macro-porosity).

555 An $SSA_{BET}$ of 378 and 340 $m^2/g$ have been measured in the M-S-H 0.8HT and M-S-H 1.2HT
556 respectively. These values are relatively high and in the same range or even greater than the
557 $SSA_{BET}$ measured for M-S-H synthesized at room temperature. The upper surface area and higher
558 volume adsorbed of M-S-H1.2HT compared to M-S-H 1.2 prepared at room temperature from
559 BET might be related to this observed $2^{nd}$ porosity difference in packing. The M-S-H 0.8
560 equilibrated at room temperature and the hydrothermally prepared HT show a substantial
561 similarity in $N_2$ sorption (size and volume of the micro-pores) and in $^{29}$Si-NMR indicating no or
562 little structural difference except the increased ordering in the sample treated at higher
563 temperature. The different micro porosity and silicate structure defined in the M-S-H 1.2HT
564 compared to M-S-H 1.2 seems to indicate a structural rearrangement during the hydrothermal
565 treatment.

566

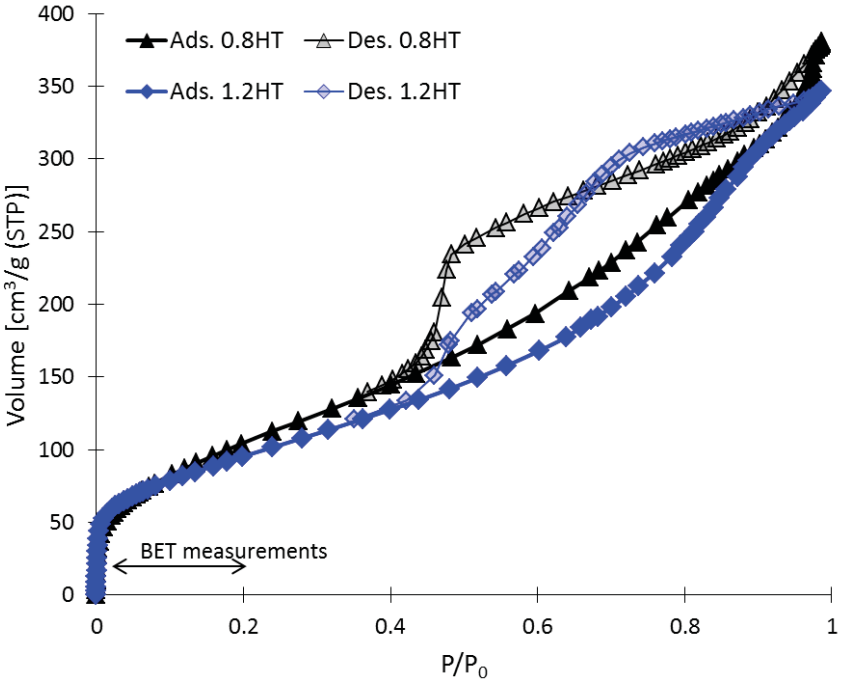


567
568 *Figure 12: $N_2$ absorption-desorption isotherms of the hydrothermally treated M-S-H.*

569

570 ## 3.2. Water in M-S-H

571 Crystalline phyllosilicates, such as talc, which represents 2:1 structure, and serpentines (1:1
572 structure) are composed of theoretically infinite silicate layers and hydroxyl groups are only
573 linked to the magnesium, the so-called inner OH, and surface OH groups as detailed in Figure 1.

Some phyllosilicates such as sepiolite or amphibole also contain zeolitic water and water coordinated to charge balancing cations, water which is more confined than zeolitic water, while smectites contain water confined in the interlayer and at the surface. M-S-H contains between 1 and 2.5 $H_2O$ per silicon based on TGA measurements ([15, 16, 22]), thus significantly more water than talc, antigorite or clay minerals. Water in M-S-H was found to be present both as adsorbed water and within the structure as $H_2O$ and hydroxyl groups ([15, 18]). In the following, the distribution of the water in the structure of M-S-H is investigated by different techniques.

### 3.2.1. $^{1}H$-$^{29}Si$ CP MAS-NMR spectroscopy

The variation of the contact time in $^{1}H$-$^{29}Si$ CP MAS-NMR (cross polarization magic angle spinning NMR) experiments allows investigating whether protons (from the hydroxide groups or water) are in the vicinity of silicate sites. The shorter the contact time, the closer a proton is. Therefore, the water adsorbed on the surface results in higher contact time than hydroxyl groups directly bound to silicon.

The $^{1}H$-$^{29}Si$ CP MAS-NMR spectra of M-S-H synthesized at room temperature, and hydrothermally prepared M-S-H recorded with varying contact times between 0 and 5 ms and the associated absolute intensities are shown in Figure 13 and Figure 14. The intensities of $Q^1$ and $Q^2$ site reached a maximum at a contact time between 2 and 4 ms, which indicated the presence of protons in the second or third coordination shell. From the geometry, the $Q^1$ and $Q^2$ silicate sites are present at the surface as Si-OH confirming the hydroxyl groups are linked to the $Q^1$ and $Q^2$ silicate sites as already observed by Nied et al. [15].

The $Q^3$ sites showed a higher contact time of > 5 ms, which indicated that the $Q^3$ silicate sites were not directly linked to hydroxyl groups but that the protons were in further distant coordination spheres such as hydroxyl groups bound to magnesium or sorbed water.

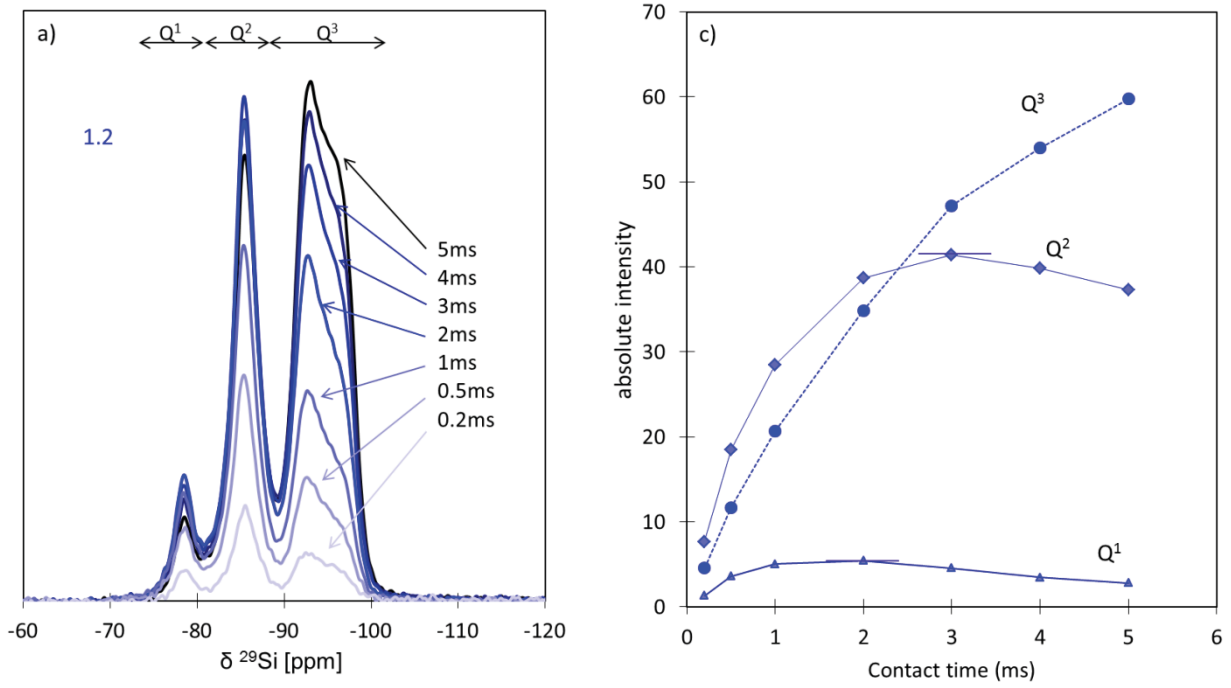

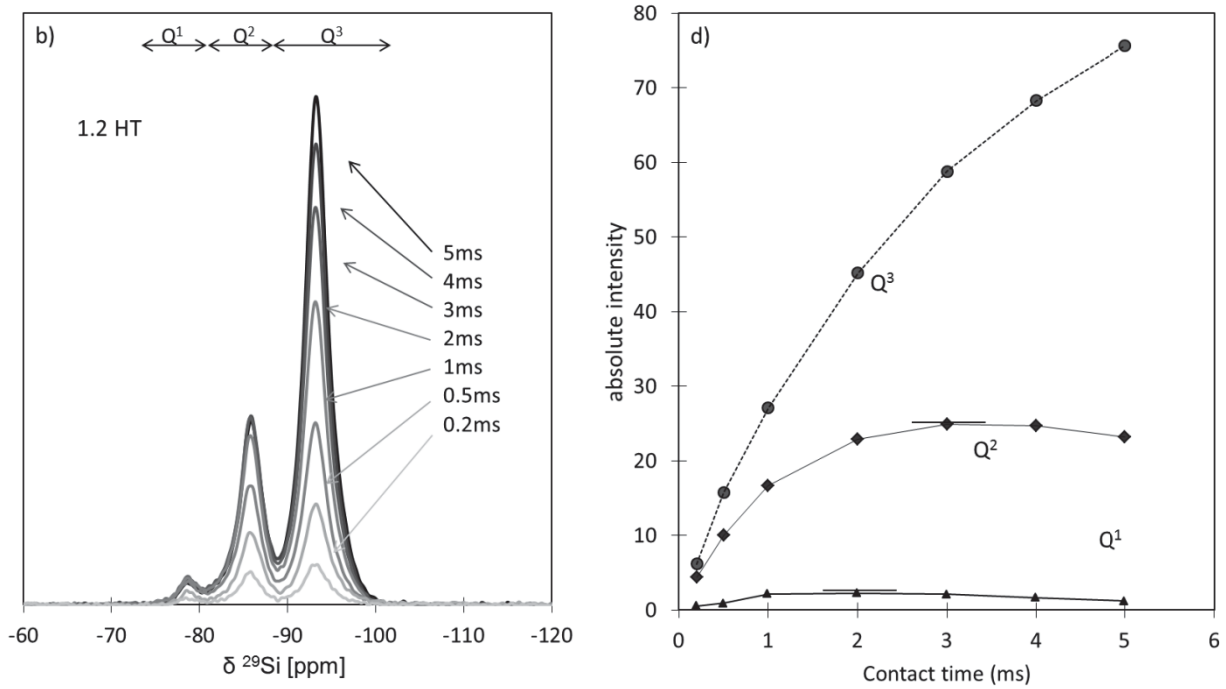


599
600 *Figure 13: $^{1}H$-$^{29}Si$ CP MAS-NMR spectra at different contact time for a) the M-S-H 1.2 sample (3.3 years 20°C),*
601 *b) the hydrothermally treated M-S-H 1.2 sample c) and d) absolute intensities associated as a function of the*
602 *different contact times.*

603

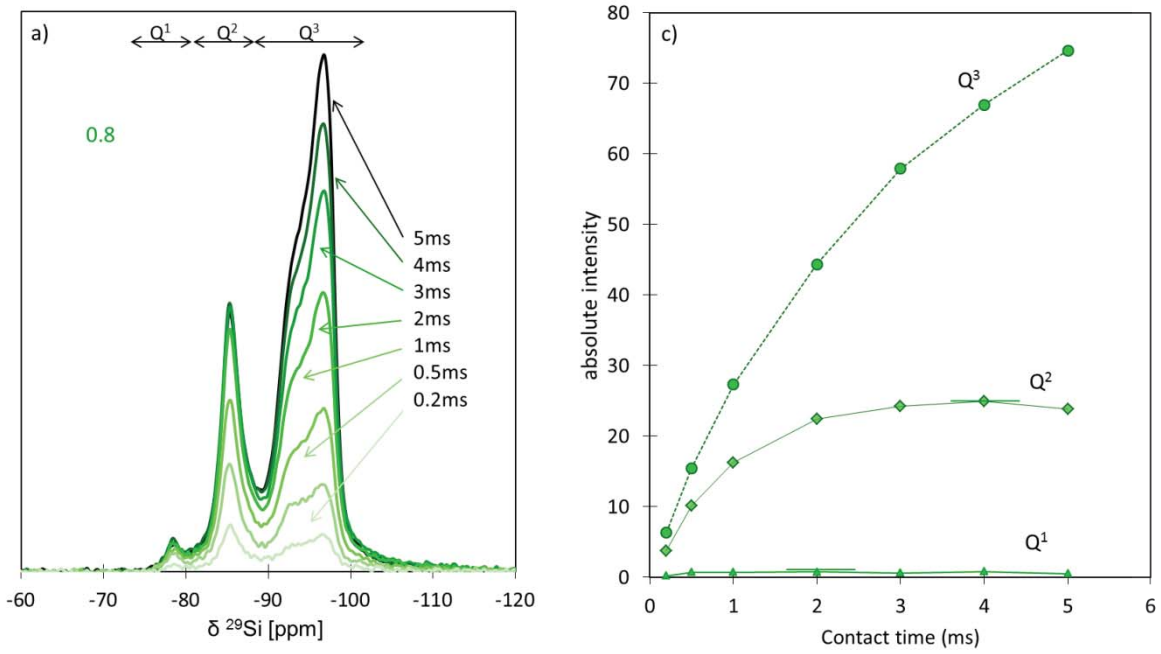


604

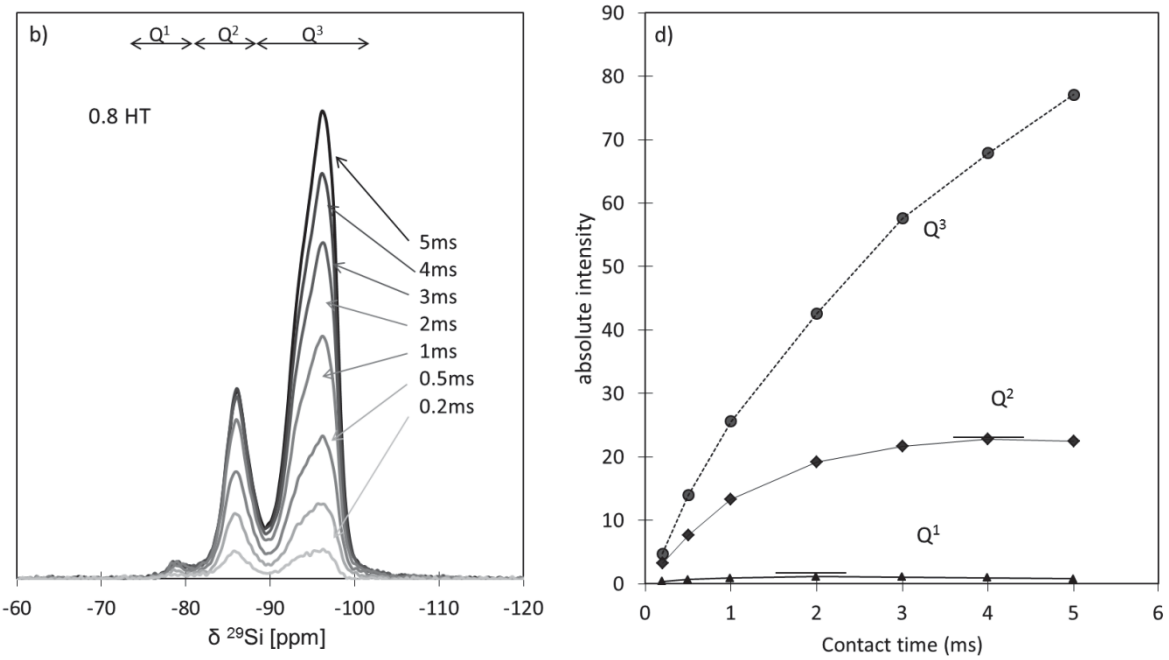


*Figure 14: $^{1}H$-$^{29}Si$ CP MAS-NMR spectra at different contact time for a) the M-S-H 0.8 sample (3.3 years 20°C), b) the hydrothermally treated M-S-H 0.8 sample c) and d) absolute intensities associated as a function of the different contact times.*

### 3.2.2. Infrared (FTIR) of hydroxyl vibrations

The FT-IR spectra recorded between 2600 and 3800 $cm^{-1}$ on M-S-H with varying Mg/Si are presented in Figure 15a and compared with spectra of 2:1, 1:1 phyllosilicates, amorphous silica, and brucite in Figure 15b. The M-S-H 1.3 contained some residual brucite (~ 2 mass% of brucite normalized to 100 g dry mass, quantified by TGA), which can be seen by the presence of the band at 3698 $cm^{-1}$ [73] and in comparison with the spectra in Figure 15b. The band (shoulder) at 3680 $cm^{-1}$ has been assigned to Mg-OH stretching vibrations in M-S-H [15, 67]. Else, little difference between the spectra recorded at different Mg/Si could be observed.

At lower wavenumbers, an overlapping of large bands corresponding to OH stretching vibrations of water molecules is found. The first band at ~ 3550-3600 $cm^{-1}$ has been attributed in sepiolite to water coordinated to magnesium ($Mg\text{-}OH_2^+$), i.e., to water at the edges of the channels [74]; this kind of water is also observed in antigorite (Figure 15b). The presence of coordinated water is typical for well-crystalline minerals. Its observation in the poorly ordered M-S-H may be explained by the presence of very confined water molecules close to the octahedral layer in M-S-H. Indeed, Lin et al. [67] observed two types of water coordinated to magnesium in an M-S-H-like phase, the first one is described as adsorbed water on magnesium located at the edge of the layer (with a water loss at 90°C in TGA) and the second one adsorbed water on magnesium located in the silicates defects (with a water loss at 140°C). Furthermore, the similarities between M-S-H and antigorite observed by PDF analysis tend to confirm the presence of coordinated water in the M-S-H.

Hair [75] reported that OH stretching of dried silanol groups at 3747 $cm^{-1}$ cannot be seen in the presence of adsorbed water and instead a “wet” silanol groups band is observed at 3660 $cm^{-1}$ and

water sorbed on those hydroxyls at 3450 $cm^{-1}$ (see Figure 35). The spectrum of the hydrated amorphous silica freeze dried and kept at 33% RH showed only the band at 3450 $cm^{-1}$ and possibly a band at 3660 $cm^{-1}$ (Figure 15b). Finally, the FT-IR spectra showed a trace of ethanol from the washing process.

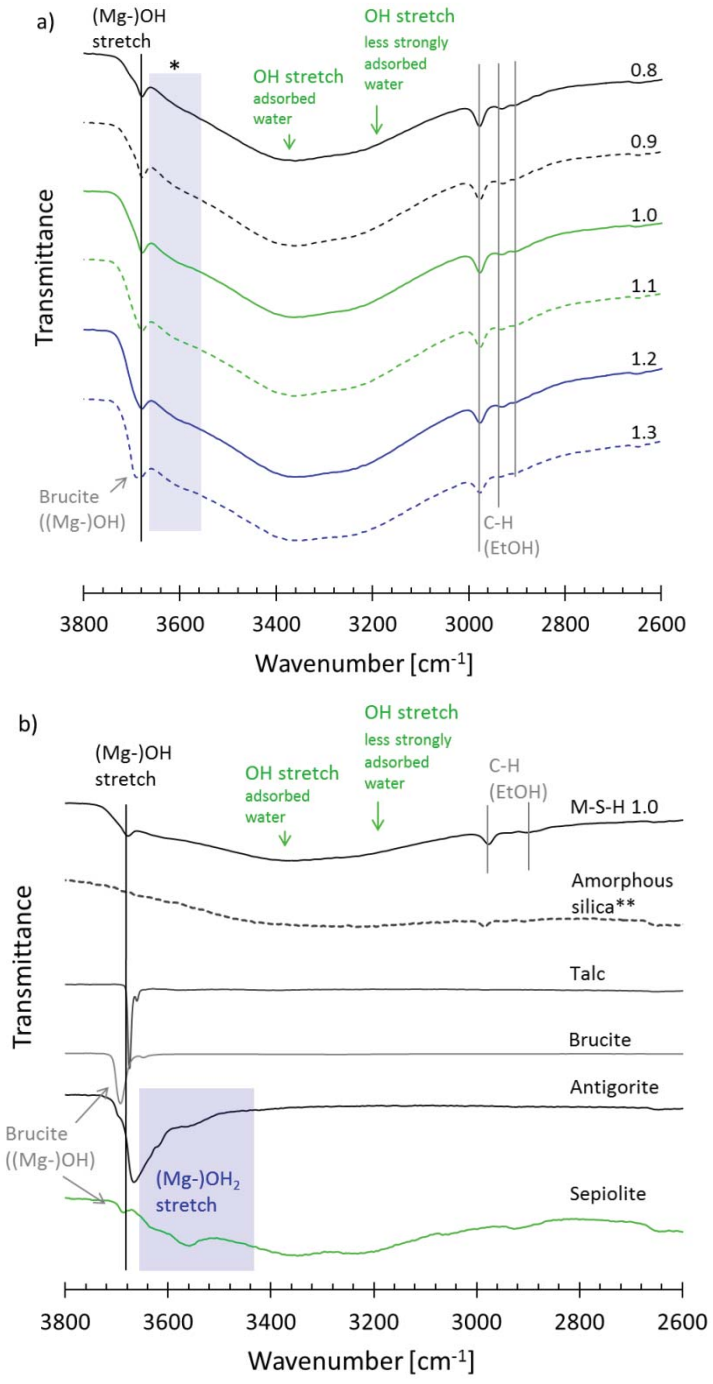


*Figure 15: a) FT-IR spectra of the M-S-H samples (3.3 years, 20°C); b) FT-IR spectra of minerals from [22] (the intensities of the spectra have been modified to fit the figure); both are zoomed between 2600 and 3800 $cm^{-1}$ and the Assignments of the stretching bands according to minerals comparison [73, 76]; *vibrations between 3600 and 3700 $cm^{-1}$ (Si-)OH · · OH2 stretch [Amorphous silica [75]] or (Mg-)$OH_2$ stretch [Sepiolite [74]or M-S-H [67]]; **amorphous silica, hydrated, washed and freeze dried and kept at 33% RH.*

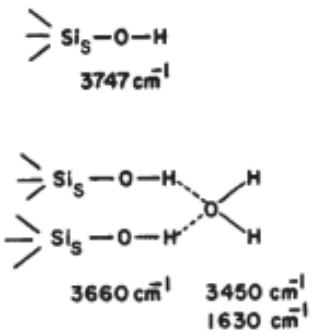


*Figure 16: Re-hydration of silica surface (reproduced from [75]).*

The FTIR data indicated that M-S-H phases contain hydroxyl groups bound directly to the silicon and magnesium, but also a significant amount of physically bound and adsorbed water, in agreement with $^{1}$H MAS NMR (40kHz) data from literature [15] and our observations by $^{1}$H-$^{29}$Si CP MAS NMR spectroscopy. The presence of coordinated water bound to magnesium might be possible. The dependence of the number of water molecules on the RH is further probed by dynamic vapor sorption (DVS) experiments and the different nature of the physically bound water by $^{1}$H NMR relaxometry measurements coupled to TGA.

### 3.2.3. Dynamic vapor sorption (DVS)

The results of the DVS measurements for M-S-H 0.9 and M-S-H 1.2 are shown in Figure 17. The sorption curves show a hysteresis, as characteristic of microporous materials such as C-S-H [77] or clay minerals [78] which confirms the presence of the micro-pores observed by the $N_2$ physio-sorption measurements.

Compared to C-S-H, where the content of water is relatively constant between 20 and 70% RH [77], the curve of M-S-H shows a gradual increase from 0 to 90% RH. This gradual increase of water in M-S-H would be consistent with the dependence of the interlayer distances (and hence water absorbed in them) on the RH as observed by XRD and with the behavior of swelling clays such as saponite or montmorillonite [78].

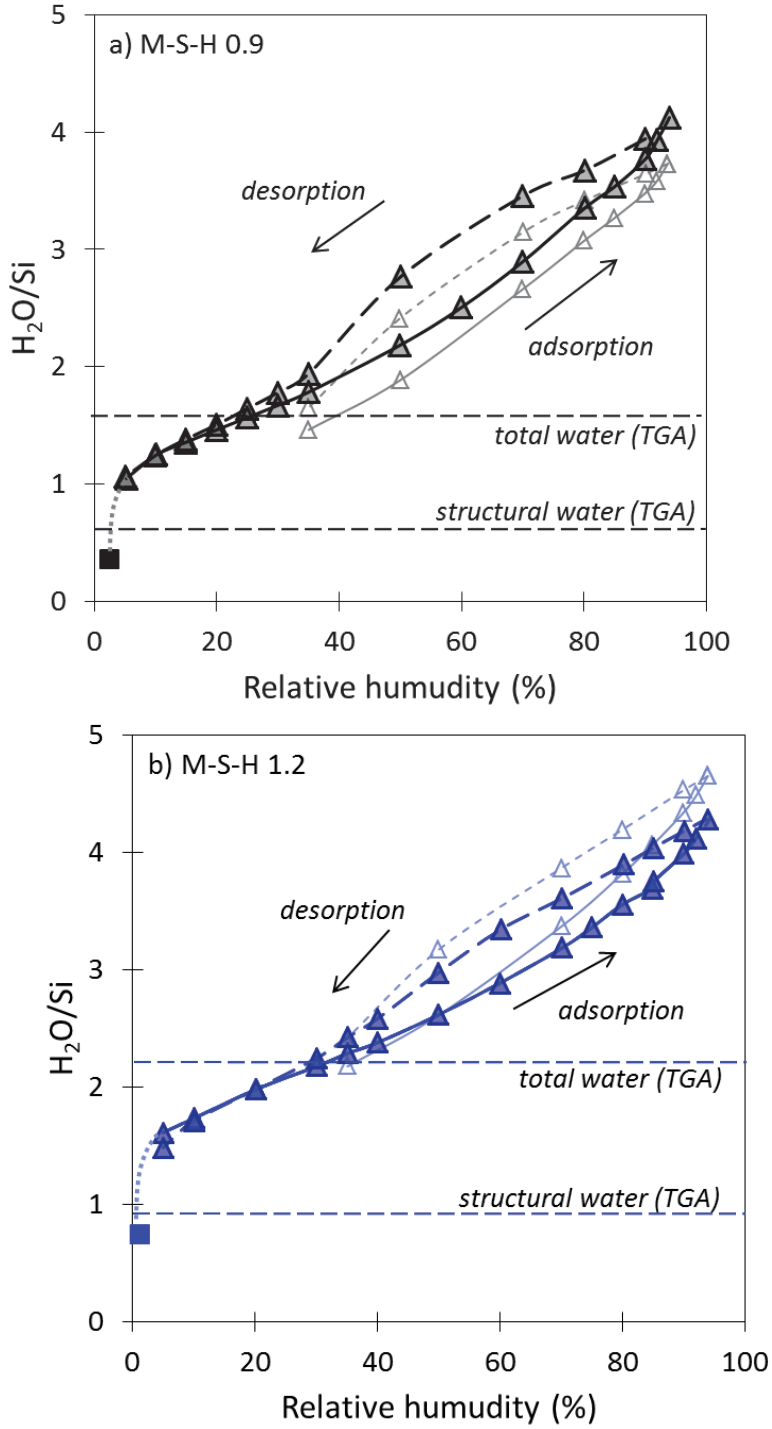


664

665
666 *Figure 17: Water vapor isotherms (adsorption and desorption) of the a) M-S-H 0.9 and b) M-S-H 1.2 (20°C, 2*
667 *years: light and empty symbols; 3.3 years: dark symbols). The squares correspond to $H_2O$/Si in the sample at <*
668 *2.5 %RH measured by DVS (structural water), the horizontal dashed lines to the to the $H_2O_{tot}$/Si total water*
669 *and to the $H_2O_{OH}$/Si structural water in M-S-H measured by TGA (see Table 6).*
670

671 The mass at the end of the DVS experiment (drying to 0% RH at 105°C during 1 day) could be
672 expected to correspond to the dry mass of the M-S-H (M-S-H with structural hydroxyl groups,
673 but without hydroxyl groups or adsorbed water at the surface). In fact, the water content

quantified by DVS after drying to 0% RH at 105°C was lower than the content of hydroxyl groups found by TGA and $^{1}$H-NMR relaxometry (as below). This is in agreement with the observation of weakly bound hydroxyl groups at the surface of the silicate layers, which are dehydroxylated at low temperatures [79] or coordinated water bound to magnesium [67].

### 3.2.4. Thermogravimetric analysis (TGA)

The TGA curves and the derivative weight losses of M-S-H aged at room temperature for 3.3 years with Mg/Si = 0.8 and 1.2, and hydrothermally prepared M-S-H are shown in Figure 18. Three water loss regions characteristic for M-S-H can be seen.

The first water loss region between 30 °C and 250 °C observed for M-S-H synthesized at room temperature had been related to poorly (physically) bound water adsorbed on the surface (monolayer, multilayers and and/or in the interlayer) of the M-S-H [15, 18]. This water loss may also include the bulk water at high RH as TGA cannot distinguish clearly between the different types of physically bound water and the bulk water. The intensity of these low-temperature losses depends on the drying and the RH of the samples (Table 4) as also observed for C-S-H [77, 80]. Two samples, M-S-H 0.9 and 1.2, had been freeze dried and re-equilibrated in a desiccator at ~85 %RH for 4 months.

*Table 4: Total bound water and hydroxyl content (molar) per silica from TGA in M-S-H equilibrated at 33% RH and 85% RH (250-980°C:* OH/Si *hydroxyl groups, 30-980°C:* $H_2O_{total}$/Si *total bound water).*

| Samples equilibrated at | | 33% RH | | | | 85% RH | |
|---|---|---|---|---|---|---|---|
| | Mg/Si | 0.9 | 1.0 | 1.1 | 1.2 | 0.9 | 1.2 |
| TGA | $H_2O_{total}$/Si | 1.58 | 1.84 | 2.01 | 2.19 | 2.44 | 3.12 |
| | OH/Si | 1.29 | 1.52 | 1.69 | 1.88 | 1.31 | 1.85 |

The second and third water losses (>250°C) have been attributed to silanol and/or magnesium hydroxyl groups in M-S-H [15, 16, 18], but may also comprise water present as a monolayer on the M-S-H surface [15]. The second water loss in M-S-H 0.8 is centered at 390°C and relates mainly to the dehydroxylation of silanol (Si-OH) groups [79], while the third weight loss at 500°C is related to the dehydroxylation of magnesium hydroxyl groups (Mg-OH). The M-S-H 1.2 seems to show only one relatively significant water loss centered at 450°C which is due to the higher content of Mg-OH and the presence of more Si-OH. Zhuravlev [79] reported the dehydroxylation of bridged hydroxyl groups at the surface of amorphous silica between 180 to 400°C, while the internal hydroxyl groups of the silica condensed only at around 900°C. The dehydroxylation of the minerals of the serpentine group (hydroxyl groups linked to the magnesium: inner OH and surface OH as detailed in Figure 1) has been observed by TGA at 670-900°C [81], while the inner OH groups linked to the magnesium in the talc structure dehydroxylates at 750-1000°C [34], in agreement with the weight loss observed for M-S-H at 850 to 900°C.

The M-S-H synthesized at room temperature contained thus hydroxyl groups bound to silicon and magnesium, in inner and surface position. The gradual and almost continuous water loss compared to brucite with a sharp water loss of its hydroxyl groups at 410°C confirms the nano-crystalline character of M-S-H. Finally, the loss of the hydroxyl bound to magnesium at 450°C rather than at 700°C indicates less order in the octahedral layers of M-S-H than observed in serpentine minerals.

The TGA curves of the hydrothermally prepared M-S-H showed the same three water loss regions. The content of the physically bound water in the hydrothermally treated M-S-H seems more structured with a shoulder at 160°C. It is unclear whether this shoulder is associated to strongly physically bound water, i.e., very confined water, or whether this shoulder is already related to dehydroxylation of silanol groups. This shoulder might also be related to the loss of coordinated water as described for hydrated magnesium silicate gels [67] or sepiolite. The overlap of water losses from the dehydroxylation is centered at 550°C for the hydrothermally prepared M-S-H instead of the 450°C indicating a better structuring.

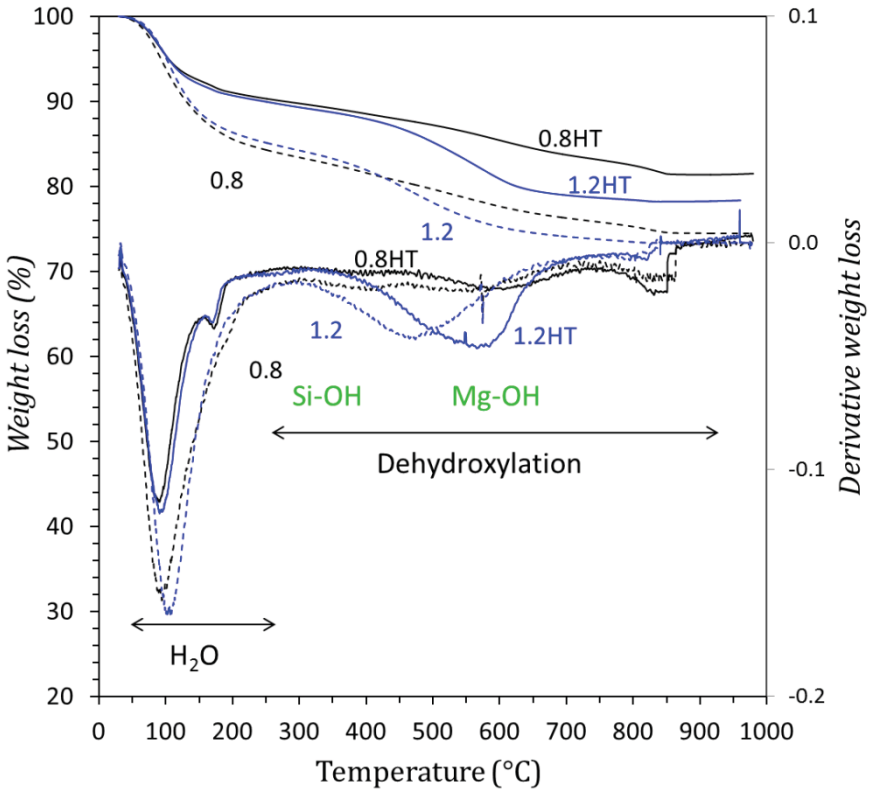


*Figure 18: Thermogravimetric analysis (TGA) of hydrothermally prepared M-S-H samples compared to M-S-H samples with similar Mg/Si.*

The repartition between physically bound water (30-250°C) and hydroxyl groups (250-900°C) quantified by TGA is shown in Figure 19 as $H_2O$/Si molar ratios. The samples equilibrated at higher RH showed a comparable amount of hydroxyl groups but much more physically bound water. Table 4 summarizes the content of the total water and hydroxyl per silicon. The total bound water and of hydroxyl groups increases with Mg/Si in M-S-H as previously reported [15, 16].

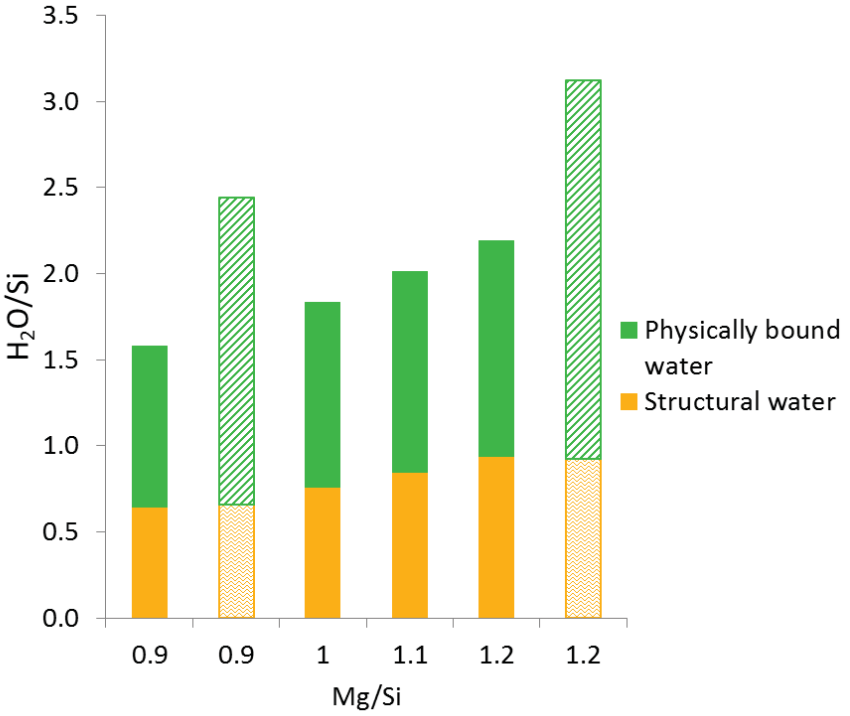


*Figure 19: Repartition between water and hydroxyl groups in M-S-H as function of the Mg/Si quantified by TGA, physically bound water (30-250°C) and hydroxyl groups (250-900°C) (samples equilibrated at ~33% RH (plain columns) and ~85% RH (patterned columns)).*

### 3.2.5. $^{1}$H NMR relaxometry

$^{1}$H NMR relaxometry measurements were performed on the two M-S-H samples Mg/Si=0.9 and 1.2 re-equilibrated at ~85% RH.

The fraction of structural water corresponding to hydroxyl groups can be accessed using the QE pulse sequence. The content of structural water and physically bound water obtained by QE is compared to the TGA results in Figure 20. The sum of QE (solid+mobile) has been normalized to the total bound water quantified by TGA. The results were in good agreement and showed that both QE and TGA could well differentiate the structural water from the physically bound water.

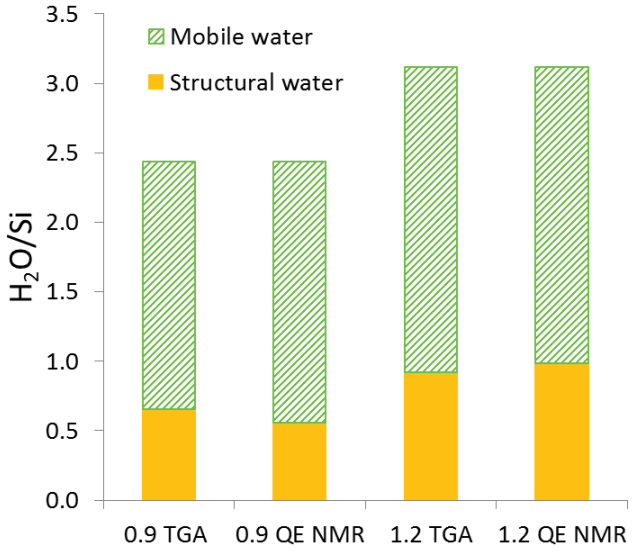


*Figure 20: Comparison of the repartition between water and hydroxyl groups in M-S-H as function of the Mg/Si quantified by TGA, physically bound water (30-250°C) and hydroxyl groups (250-900°C) and the deconvolutions of the QE-NMR recordings (samples equilibrated at 85% RH ).*

As shown in Figure 2, different $T_2$ relaxation times (~0.05 ms, ~0.8 ms, and > 6 ms) were observed which are assigned to: *very confined* water, *confined* water (both physically bound water) and bulk water. The average specific $T_2$ relaxation times obtained by inverse Laplace transform (ILT) are given in Table 5. The results obtained at 33% RH showed similar first relaxation time (*very confined* water), but a shorter relaxation time for the *confined* water. This result, although prone to the error associated with the overall low signal at low RH, indicates a more *confined* water at lower RH and is consistent with the XRD results where the basal spacing was observed to decrease with the RH.

*Table 5: Specific $T_2$ relaxation times obtained by ILT for the M-S-H samples equilibrated at 33 and 85% RH.*

| M-S-H | Very confined water ms | | Confined water | | Bulk water | |
|---|---|---|---|---|---|---|
| 0.9 85% RH | 0.056 | *±0.036* | 0.769 | *±0.043* | 12.6 | *±2.58* |
| 1.2 85% RH | 0.049 | *±0.015* | 0.821 | *±0.014* | 6.80 | *±3.84* |
| 0.9 33% RH | 0.072 | *±0.017* | 0.345 | *±0.017* | 3.80 | *±21.00* |
| 1.2 33% RH | 0.048 | *±0.034* | 0.342 | *±0.053* | 2.04 | *±1.11* |

*± corresponds to the 95% confidence interval.*

Figure 21 shows the repartition of water quantified by the QE (structural water) and multi-exponential fitting of the CPMG (physically bound water and bulk water) normalized to the mobile water found by the QE and the total bound water determined by TGA for the samples at 85% RH. The calculations gave similar results as the TGA (see Figure 19, patterned columns) for the repartition between physically bound and structural water (hydroxyl groups). However, unlike TGA or QE, CPMG can differentiate between the different populations of water such as *very*

*confined* water (probably the strongly adsorbed water), *confined* water and bulk water. The $^{1}H$ NMR relaxometry showed that the content of bulk water is low (<3% of the total water) which is in fact at the level of the background noise. The content of *confined* water, i.e. the water present in very fine pores, is about 65 and 56 % of the total water for the 0.9 and 1.2 M-S-H samples, while the amount of *very confined* water was around 10%. At higher Mg/Si the content of *very confined* water ($T_2$ ~0.05 ms) per silica increased (Table 6), however, if the water content is expressed per magnesium (Appendix B) the content of water remains relatively constant.

It should be however noted that due to the short $T_2$ (at ~0.05 ms) of this first peak of the CPMG assigned to *very confined* water, may not resolve all possible water, or artificially overestimate the position of the first peak. This is because the first echo was at 0.05 ms and consequently only part of the decay from the lowest peak could be resolved in the range of echoes of 0.05 -12 ms applied here.

The *very confined* water could include water in the interlayers (internal water) and water strongly adsorbed on the surface of the particle (external water), possibly also the coordinated water bound to magnesium as discussed previously. At both Mg/Si ratios investigated, the *very confined* water corresponded to approximately 10% of the signal, indicating the presence of more *very confined* water per Si at higher Mg/Si ratios.

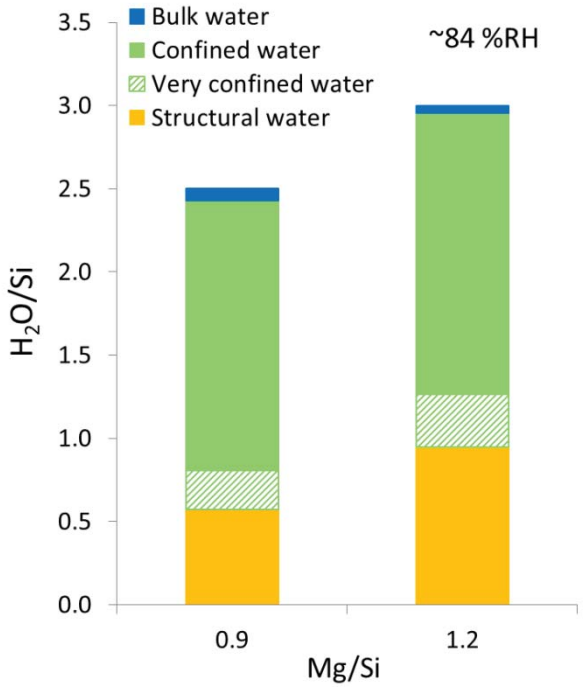


*Figure 21: Repartition of the water in M-S-H normalized by the total bound water quantified by TGA as a function of the Mg/Si (structural water from the QE, mobile water from the CPMG.*

The samples equilibrated at 33%RH showed more of very confined water and less of confined water that the samples at 85% RH. The increase of the relative humidity of the sample fills the pore between particle and the first layers of water on the surface (very confined water) are shown

as less confined as soon as the pores are full (based on the assumed model of fast exchange of the water molecules between the zone close to the solid surface and bulk of the pore [60].

It might be postulated that the slightly increasing *very confined* water content at higher Mg/Si is due to: a) higher strongly adsorbed water content on the surfaces of silicates, b) higher coordinated water content to magnesium i.e., to water coordinated at the edges and/or, c) more *very confined* water in the smaller interlayer space. Indeed, the water of a nano-pore might be described as only *very confined* water where the water of a slightly bigger pore might be described in both *very confined* and *confined* water resulting with a higher content of *very confined* water in smaller pores.

*Table 6: Total bound water and hydroxyl content (molar) per silica in M-S-H from DVS measurement, from TGA and from the $^1$H NMR relaxometry. The results are normalized to the total bound water quantified by TGA (errors in TGA ± 12%; DVS ± 10 %; $^1$H NMR ± 17%).*

| | | 0.9 | | | 1 | 1.1 | 1.2 | | |
|---|---|---|---|---|---|---|---|---|---|
| samples equilibrated at | | 33% | 85% | 94% | 33% | 33% | 33% | 85% | 94% |
| DVS | $H_2O$/Si (ads) | 1.78 | 3.53[a] | 4.12 | | | 2.28 | 3.75[a] | 4.28 |
| | $H_2O$/Si (des) | 1.94 | 3.67[a] | | | | 2.42 | 4.04[a] | |
| | OH/Si (structural) [b] | 0.72 | | | | | 1.48 | | |
| TGA | $H_2O$/Si | 1.58 | 2.44 | | 1.84 | 2.01 | 2.19 | 3.12 | |
| | OH/Si (structural) [c] | 1.29 | 1.31 | | 1.52 | 1.69 | 1.88 | 1.85 | |
| H NMR | bulk water/Si | *0.07*[d] | 0.07 | | | | *0.06*[d] | 0.05 | |
| | confined water/Si | *0.54*[d] | 1.58 | | | | *0.56*[d] | 1.75 | |
| | very confined water/Si | *0.50*[d] | 0.23 | | | | *0.69*[d] | 0.33 | |
| | OH/Si (structural) | *0.93*[d] | **1.12** | | | | *1.77*[d] | **1.97** | |
| CEC | $Mg^{2+}$/Si | 0.022 | | | 0.025 | 0.028 | 0.030 | | |

[a] *From the DVS measurements of the M-S-H equilibrated at 33% RH;* [b] *two times the $H_2O$/Si quantified in the sample at <2.5 RH%;* [c] *structural water plus possibly strongly adsorbed water;* [d] *the results have been re-normalized considering the signal due to bulk water with very large relaxation time (> 2 ms) as noise.*

### 3.2.6. Discussion

The DVS measurements indicated that the amount of total water in M-S-H increased clearly with the RH and fill the microporosity of the particles. TGA and DVS indicated the presence of more physically bound water at higher RH. This physically bound was resolved by $^1$H-NMR relaxometry as *confined* water present in the micro-pores even at 85% RH, while hardly any bulk water was found at this RH. DVS, TGA and $^1$H-NMR relaxometry measurements indicated a relatively similar amount of physically bound water per magnesium in M-S-H independent of Mg/Si, which translated into a higher $H_2O$/Si at higher Mg/Si in M-S-H (Table 6).

A significant amount of hydroxyl groups (structural water) is also present in M-S-H, and the number of hydroxyl groups quantified by DVS, TGA and $^1$H-NMR relaxometry increased with the Mg/Si in M-S-H (Table 6 and Appendix B). $^1$H-NMR relaxometry data indicated that the amount of OH/Si nearly duplicated from Mg/Si = 0.8 to 1.2 (Table 6), while the difference in the amount quantified by TGA was less distinct, due to the substantial overlap of the different signals. Also, the $^{29}$Si MAS NMR data indicated the presence of more $Q^1$ and $Q^2$ silicates which exhibit Si-OH groups (predominantly protonated, details in section 3.3) at higher Mg/Si (Table

6). As also the content of hydroxyl groups per magnesium increased with the Mg/Si (Appendix B), not only more hydroxyl groups are bound to the silicate at high Mg/Si but also more Mg-OH groups are present.

## 3.3. Surface properties

Swelling phyllosilicates such as montmorillonite or saponite exhibit a negatively charged surface due to the partial replacement of silicate by aluminate in the tetrahedral silicate layers. Cations are present in the interlayers and/or external surface to compensate these negative charges. The basal spacing depends on the nature of the counterion and its wettability.

Amorphous silica shows a negative zeta potential at pH values from 3 to 10 [82], due to the deprotonation of surface silanol groups, while brucite exhibits positive zeta potential of approximately 20 mV in the pH range 3-10 [82]. Pokrovsky and Schott [83] found, by studying zeta potential of brucite as a function of the pH, a PZC (point of zero surface charge) of around 11, confirming that below this value, brucite has a positive effective surface charge (Figure 22).

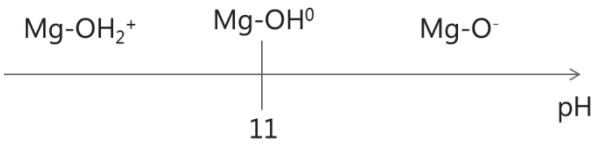


*Figure 22: Schematic brucite surface charge in function of the pH (adapted from [83]).*

Antigorite exhibits an intermediate only slightly negative zeta potential, indicating a contribution of both the positive magnesia-hydroxyl octahedral layers and the negative silica tetrahedral layers [82]. In contrast, chrysotile with a comparable chemical composition exhibits a positive zeta potential as its needle like structure exposes magnesium hydroxide on the exterior surface [82, 84].

### 3.3.1. CEC

The cation exchange capacity (CEC) is a measure of the amount of exchangeable cations present either at the surface (in the Stern and diffuse layer) or interlayer of the solid particle. The CEC quantifies the cations filtrated with the solid which charge-balance the surface charge of the solid and corresponds thus to the surface charge density.

A positive CEC has been measured for M-S-H, as shown in Figure 23, which indicates the presence of exchangeable cations in its structure and thus a negative surface charge of M-S-H as in phyllosilicates. The measured CEC increased from ~ 35 meq/100g at pH from 8.3 (Mg/Si = 0.8) to ~ 40 meq/100g at pH 10 and Mg/Si = 1.2. This observation confirmed the presence of hydroxyl surface groups like in amorphous silica and brucite that experience deprotonation upon pH increase. As CEC measures the overall amount of exchangeable cations, it is well possible that in addition to the negatively charged $SiO^-$ also some $Mg\text{-}OH_2^+$ surface sites were present, although less than the negatively charged silanol groups.

The kind and amount of cations present on the CEC sites were also measured; mainly magnesium was present plus 1 to 2 % sodium, which was present as an impurity in the starting materials. The presence of only 1 to 2% of $Na^+$ on the CEC sites, although similar magnesium and sodium concentrations in solution were measured (Table 1), showed that the sorption of the bivalent $Mg^{2+}$ is favored compared to the monovalent $Na^+$, which is commonly observed on silica (see e.g. [85-87]). The CEC measured by the total of the cations released by the cobalt(III) replacement agreed well with the total CEC measured by colorimetry, indicating that the M-S-H phases did not dissolve significantly.

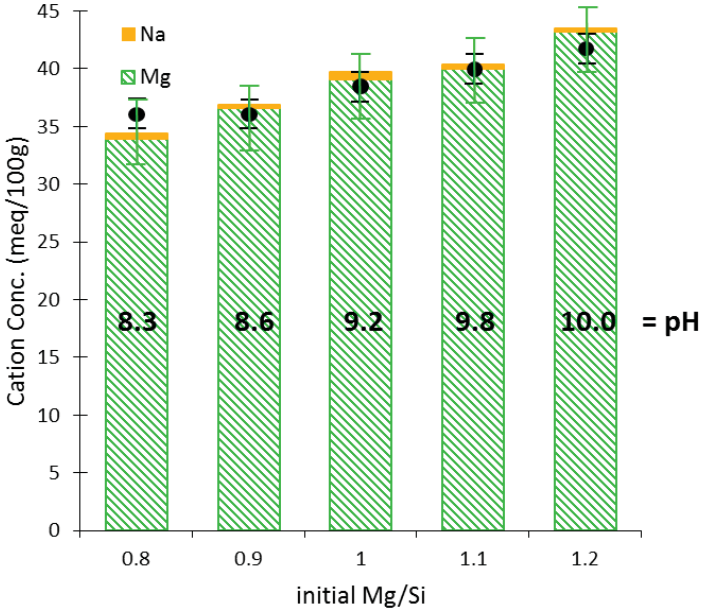


*Figure 23: Cation exchange capacity (CEC) measured by colorimetry (black circles) and concentrations of cations sorbed on M-S-H samples (2 years- at 20°C) measured by cobalt hexamine method as a function of the initial Mg/Si.*

The amount of magnesium at the cation exchange sites was related to the total amount of magnesium present in Table 6. Only 2 to 3% of the total magnesium was present on the cation exchange sites of M-S-H.

The total of exchangeable cations in M-S-H was higher than the CEC of sepiolite (~ 10 meq/100g) [88] but lower than the CEC of e.g. saponite (~ 70-150 meq/100g) (e.g., [89, 90]), where Al and Fe replace a fraction of Mg and Si in the structure.

### 3.3.2. Zeta potential

The zeta potential measures the charge of a particle not directly at the surface but in some distance, such that (cat)ions near the surface in the Stern and even some in the diffuse layer, appear as part of the solid [61, 84, 91]. Thus the presence of more magnesium in the cation exchange sites of M-S-H can result in less negative zeta potential measurements. The zeta potential measurements on M-S-H particles, as shown in Figure 24, indicate a decrease from -19 mV at pH 8.6 to -28 mV at pH 10.2. The zeta potential of hydrated amorphous silica was ~ -43 mV at pH of 6.5 which corresponds well with literature data [82], while the zeta potential of brucite was positive ~ 2 mV at pH = 10.5 and is expected to be higher at lower pH values [83].

The negative effective charge of M-S-H confirms that the Si-OH groups on the $Q^1$ and $Q^2$ silicates are at least partially deprotonated: $Si\text{-}O^-$ and that the low cation concentrations in solution did not fully balance these negative charges, i.e. not all the charge balancing cations are in the Stern layer but at last a part in the diffuse layer. The decrease in zeta potential from pH 8 to 9 is probably related to the progressive deprotonation of silanol groups as the pH increases and magnesium concentrations decreases. The trend, more negative values at higher pH values and thus at higher Mg/Si agree well with the CEC measurements.

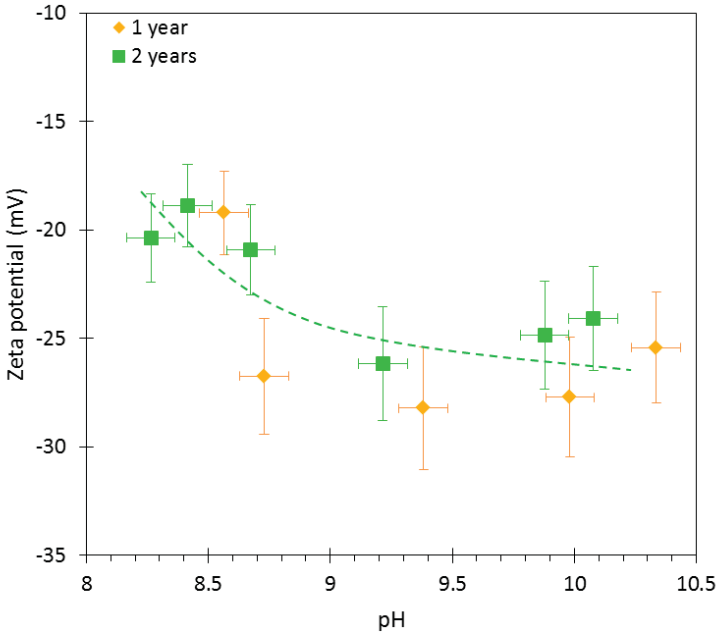


*Figure 24: Zeta potential of M-S-H with Mg/Si=0.8-1.2 as a function of pH, M-S-H particles aged of 1 and 2 years at 20°C, the line is only guide to eye.*

### 3.3.3. Effect of filtration on measured pH values

The presence of charged particle surfaces also affected the pH measurements; the pH of the filtrated liquid was systematically lower than the pH measured in the corresponding suspension as detailed in Table 7. The decrease of pH due to the filtration indicated that not only $Mg^{2+}$ but also $OH^-$, probably as $MgOH^+$, was associated with the surface of M-S-H. In fact, in the pH range 8-10, the fraction of $MgOH^+$ becomes more important as the pH increases (Figure 25). The $OH^-$/Si filtrated with the solid shown in Table 7 was calculated from the pH differences between the suspension and the corresponding filtrated supernatant. It indicates that the content of $MgOH^+$ counter-ions is very low (0.01 to 2% at pH 9.9) compared to the amount of $Mg^{2+}$ found on the cation exchange sites (Table 6), which is in agreement with the fractions of $MgOH^+$ and $Mg^{2+}$ in the solution shown in Figure 25.

*Table 7: pH measured in the M-S-H samples after 3.3 years at 20°C.*

| initial Mg/Si | pH measured in suspension | pH measured in filtrated solution | [OH] filtrated with the solid (mmol/l) | OH filtrated with the solid / Si* |
|---|---|---|---|---|
| 0.7 | 8.3 | 8.0 | 0.0007 | 0.000003 |
| 0.8 | 8.3 | 7.9 | 0.0008 | 0.000003 |
| 0.9 | 8.5 | 8.2 | 0.0011 | 0.000005 |
| 1.0 | 9.1 | 8.8 | 0.0043 | 0.00002 |
| 1.1 | 9.7 | 9.1 | 0.0255 | 0.00012 |
| 1.2 | 9.9 | 9.6 | 0.0269 | 0.00013 |
| 1.3 | 10.3 | 10.0 | 0.0675 | 0.00034 |

| | | | | |
|---|---|---|---|---|
| 1.4 | 10.4 | 10.1 | 0.0850 | 0.00045 |

* Mg on CEC: 0.02 to 0.03 Mg/Si (Table 6).

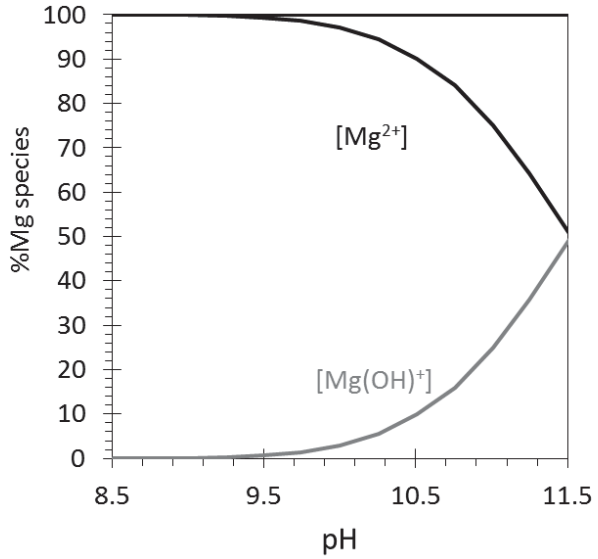


*Figure 25: Magnesium speciation ($Mg_{tot}$ = 100 mol/l) in solution at 20°C as a function of the pH.*

### 3.3.4. Discussion

The CEC measurements indicated the presence of exchangeable cations (mainly $Mg^{2+}$) at the surface of M-S-H. Its amount increased while the zeta potential decreased, when the pH raised, indicating an increase of the negative surface charge density of M-S-H with pH due to the deprotonation of the silanol groups of M-S-H.

The comparison of the CEC of 0.04 to 0.06 meq/Si (0.02 - 0.03 $Mg_{exch}$/Si) with the fraction of silanol groups of 0.3 to 0.6 per Si, indicated that only approximately 10% of the silanol groups were deprotonated in the pH range studied.

The zeta potentials measured in the M-S-H suspension were negative but decreased only moderately at higher pH values in contrast to the CEC measurements, in agreement with the presence of more $Mg^{2+}$ at the surface at higher pH values. The presence of more magnesium on the cation exchange sites of M-S-H could also explain why the amount of *very confined* water quantified by $^{1}H$ NMR relaxometry increases with the Mg/Si, as $Mg^{2+}$ in water is surrounded by 6 to 18 water molecules $Mg[H_2O]_6^{2+}[H_2O]_{12}$ [92], such the amount of water should increase strongly with the amount of $Mg^{2+}$ on the cation exchange sites. In addition, also the silanol groups are associated with additional water as observed by FTIR and $^{1}H$-$^{29}Si$ CP MAS-NMR measurements. Thus the increase of the fraction of silanol groups (as observed by $^{29}Si$ MAS NMR spectroscopy) at high Mg/Si contributes also to the presence of more adsorbed water.

## 3. Conclusions

X-ray diffraction, X-ray pair distribution function results, and $N_2$ physio-sorption data confirmed that M-S-H phases were poorly ordered and nanosized phyllosilicates as already suggested in

[16]. The presence of 30% to 55% $Q^1$ and $Q^2$ sites at low and high Mg/Si, respectively, as observed by $^{29}Si$ NMR, indicates a high fraction of silanol (Si-OH) groups present at edges sites or defects in the silicates layers. Hydrothermal treatment resulted in M-S-H with a slightly better ordered structure, as observed by $^{29}Si$ MAS NMR spectroscopy, X-ray diffraction data and TGA. In all cases, M-S-H showed a small coherence length of about 1.2 nm, as measured by X-ray PDF analyses, and a relatively high specific surface area of 300 to 500 $m^2/g$ and micro- and nano-porosity similar to poorly ordered synthetic phyllosilicates.

The samples were observed to swell slightly in the presence of ethylene glycol and the water content was highly dependent on the RH. $^1H$ NMR relaxometry performed on the samples conditioned at 85%RH, combined with TGA measurement, showed that hardly any bulk water was present, while large part of physically bound water was present in micro-pores. Also the amounts of more confined water (either present at the surface or as water associated with $Mg^{2+}$ cations) and hydroxyl groups were observed increasing at higher Mg/Si. This higher content of hydroxyl groups at high Mg/Si was related to the higher content of magnesium and thus of Mg-OH groups and to the increase of the density of silanol groups at higher Mg/Si.

M-S-H exhibited a negative surface charge indicating a partial deprotonation of the silanol groups. The small negative surface charge also leads to the presence of a low amount of magnesium on cation exchange sites (equal to 0.02 - 0.03 Mg/Si) compensating the negative charge similar as has been observed for phyllosilicates. The negative surface of the M-S-H particle might explain the weak cohesion and small particle size observed.

The different experimental techniques applied to characterize M-S-H showed a poorly order structure related to phyllosilicate with a negative surface charge, exchangeable cations and both structural and bound water types. The ill-defined and nano-sized structure of M-S-H with its large number of silanol sites resulted in the presence of exchangeable cations. The strong resemblance of M-S-H to hydrated 2:1 / 1:1 phyllosilicates could also indicate that an aluminum uptake in the octahedral and tetrahedral layers of M-S-H could be possible similar to phyllosilicates. Further investigations have been carried out to investigate the possible incorporation of aluminum in the structure.

## 4. Acknowledgments

The authors would like to thank Daniel Rentsch and Frank Winnefeld for helpful discussions, Andreas Jenni for providing reference samples, Karen Scrivener for giving access to measuring setups, and François Avet and Zhangli Hu, for help with the experiments. The solid state NMR hardware was partially granted by the Swiss National Science Foundation (SNSF, grant no. 206021_150638/1).

## 5. Appendix

*Appendix A: Details of the X-ray PDF analysis fitting.*

- ***Minerals used:***

**Sepiolite fiche CIF:** 9014723
Formula : $H_{12}\ Mg_{3.592}\ O_{22}\ Si_6$
Calculated formula: $Mg_{14.368}\ O_{68}\ Si_{24}\ Wa_{20}$
Groupe d'espace : P n c n
α=β=γ= 90° ; a=13.3067 Å ; b=26.9720 Å ; c=5.2664 Å

*Sanchez, M. , Garcia-Romero E. , Suarez, M. , Silva, I. , Fuentes-Montero L. , Martinez-Criado G.* , Variability in sepiolite: Diffraction studies Note: Sample BAT25 Note: T = 25 C, Journal of American Mineralogist, Vol. 96, pp. 1443 – 1454, (2011)

**Talc fiche CIF:** 1011152

Formule : $H_2$ $Mg_3$ $O_{12}$ $Si_4$

Groupe d'espace : C 1 2/c 1

a=5.26 ; b=9.1 ; c=18.81 ; α=γ=90° ; β=100.08°

*Gruner, J. W. ,* The crystal structures of talc and pyrophyllite, Zeitschrift fuer Kristallographie, Kristallgeometrie, Kristallphysik, Kristallchemie (-144,1977), Vol. 88, pp. 412-419, (1934)

**Antigorite-Tb (n = 17) fiche CIF:** 19084

Formule : $Mg_{48}$ $O_{147}$ $Si_{34}$

Groupe d'espace : triclinique P 1 1

Dodony I, Posfai M, Buseck P R, Revised structure models for antigorite: An HRTEM study, American Mineralogist 87 (2002) 1443-1457

a=43.5 angstroms ; b=9.23 angstroms; c=7.27 angstroms; α= 90 ; β = 92°; =γ=90°

**Antigorite-M fiche CIF:** 9014625

Formule : $Mg_{39}$ $O_{120}$ $Si_{28}$

Groupe d'espace : monoclinique P 1 m 1

a=35.02 ; b=9.23 ; c=7.27 ; α= β=γ=90°

Dodony, I.; Posfai, M.; Buseck, P. R., Revised structure models for antigorite: An HRTEM study Note: n = 14, Journal of American Mineralogist, Vol. 87, pp. 1443 – 1457, (2002)

**Chrysotile fiche CIF:** 1010960

Formule : $H_8$ $Mg_6$ $O_{18}$ $Si_4$

Groupe d'espace : C 1 2/m 1

a=14.66; b=18.5 ; c=5.33 ; α=γ=90° β=93.27°

Warren, B.E. ; Bragg, W.L., The crystal structure of chrysotile $H_4$ $Mg_3$ $Si_2$ $O_9$, Zeitschrift fuer Kristallographie, Kristallgeometrie, Kristallphysik, Kristallchemie (-144,1977), Vol. 76, pp. 201-210, (1931)

**Lizardite fiche CIF:** 0005585

Formule : $Mg_3$ $Si_2$ $H_4$ $O_9$

Groupe d'espace : P 3 1 m

a=b=5.332 ; c=7.332 ; α=β=90° ; γ=120°

*Guggenheim S. and Zhan W.* , Effect of temperature on the structures of lizardite-1T and lizardite-2H1, The Canadian Mineralogist, Vol. 36, pp. 1587-1594, (1998)

- ***Fits:***

For every fit, the Qdamp was set to 0.05 and Qmax was kept at 17, the fit range is detailed below.

| | | | 1.3 (1-20 Å) *Figure 7* | 0.8 (1-20 Å) *Figure 8* | 0.8 (1-12 Å) *Figure 9* |
|---|---|---|---|---|---|
| CIF file | Paramètre | Initial | Ajusté | Ajusté | Ajusté |
| sepiolite | Scale factor | 1 | 0.739 | 0.61 | |
| | Delta1 | 0 | 1.128 | 0 | |
| | a | 13.4 | 13.125 | 13.038 | |
| | b | 26.8 | 27.281 | 27.065 | |
| | c | 5.28 | 5.415 | 5.418 | |
| | α | 90 | 90 | 90 | |
| | β | 90 | 90 | 90 | |
| | γ | 90 | 90 | 90 | |
| | adp Mg | 0 | 0.00549 | 0.0077 | |
| | adp Si | 0 | 0.0281 | 0.012 | |
| | adp O | 0 | 0.0356 | 0.0188 | |
| | $r_w$ | | 0.61 | 0.60 | |

| | | | | | |
|---|---|---|---|---|---|
| Talc | Scale factor | 1 | 0.685 | 0.609 | 0.797 |
| | Delta1 | 0 | 1.428 | 1.497 | 1.431 |
| | a | 5.26 | 5.39 | 5.352 | 5.356 |
| | b | 9.1 | 9.357 | 9.34 | 9.24 |
| | c | 18.81 | 18.019 | 18.266 | 18.39 |
| | α | 90 | 90 | 90 | 90 |
| | β | 100 | 100 | 100 | 100 |
| | γ | 90 | 90 | 90 | 90 |
| | adp Mg | | 0.00931 | 0.018 | 0.0162 |
| | adp Si | | 0.0619 | 0.045 | 0.0606 |
| | adp O | | 0.0605 | 0.057 | 0.0564 |
| | $r_w$ | | 0.59 | 0.55 | 0.42 |
| Antigorite Tb | Scale factor | 1 | 0.849 | 0.793 | 0.865 |
| | Delta1 | 0 | 1.047 | 1.141 | 1.058 |
| | a | 43.5 | 43.437 | 43.422 | 43.442 |
| | b | 9.23 | 9.455 | 9.401 | 9.395 |
| | c | 7.27 | 7.154 | 7.077 | 7.028 |
| | α | 90 | 90 | 90 | 90 |
| | β | 92 | 92 | 92 | 92 |
| | γ | 84.75 | 84.75 | 84.75 | 84.75 |
| | adp Mg | | 0.0197 | 0.0312 | 0.0312 |
| | adp Si | | 0.0144 | 0.00701 | 0.0081 |
| | adp O | | 0.0244 | 0.0288 | 0.0269 |
| | $r_w$ | | 0.46 | 0.46 | 0.42 |
| Antigorite M | Scale factor | 1 | 0.769 | 0.546 | |
| | Delta1 | 0 | 1.237 | 0 | |
| | a | 35.02 | 34.202 | 34.709 | |
| | b | 9.23 | 9.458 | 9.32 | |
| | c | 7.27 | 7.186 | 7.335 | |
| | α | 90 | 90 | 90 | |
| | β | 90 | 90 | 90 | |
| | γ | 90 | 90 | 90 | |
| | adp Mg | | 0.0106 | 0.0274 | |
| | adp Si | | 0.0352 | 0.0113 | |
| | adp O | | 0.0441 | 0.0072 | |
| | $r_w$ | | 0.61 | 0.64 | |
| Chrysotile | Scale factor | 1 | 0.687 | 0.475 | |
| | Delta1 | 0 | 1.535 | 0 | |
| | a | 5.34 | 5.339 | 5.468 | |
| | b | 9.241 | 9.497 | 9.196 | |
| | c | 14.689 | 15.067 | 14.823 | |
| | α | 90 | 90 | 90 | |
| | β | 93.66 | 93.66 | 93.66 | |
| | γ | 90 | 90 | 90 | |
| | adp Mg | | 0.0049 | 0.025 | |
| | adp Si | | 0.0355 | 0.0032 | |

| | | | | |
|---|---|---|---|---|
| | adp O | | 0.0915 | 0.0156 |
| | $r_w$ | | 0.56 | 0.66 |
| Lizardite | Scale factor | 1 | 0.123 | 0.128 |
| | Delta1 | 0 | 0.639 | 1.379 |
| | a | 5.332 | 5.475 | 5.462 |
| | b | 5.332 | 5.281 | 5.232 |
| | c | 7.23 | 7.666 | 7.621 |
| | α | 90 | 90 | 90 |
| | β | 90 | 90 | 90 |
| | γ | 90 | 90 | 90 |
| | adp Si | | 0.0103 | 0.0079 |
| | adp Mg | | 0.00761 | 0.0196 |
| | adp O | | 0.0175 | 0.0195 |
| | adp H | | 0.000329 | 0.00033 |
| | $r_w$ | | 0.69 | 0.68 |

*Appendix B: Total bound water and hydroxyl content (molar) per magnesium in M-S-H from DVS measurement, from TGA and from the $^1$H NMR relaxometry. The results are normalized to the total bound water quantified by TGA (errors in TGA ± 13%; DVS ± 11 %; $^1$H NMR ± 19%) (calculated from (Table 6)).*

| | | 0.9 | | | 1 | 1.1 | 1.2 | | |
|---|---|---|---|---|---|---|---|---|---|
| samples equilibrated at | | 33% | 85% | 94% | 33% | 33% | 33% | 85% | 94% |
| DVS | $H_2O$/Mg (ads) | 1.98 | 3.92 [a] | 4.58 | | | 1.90 | 3.13 [a] | 3.57 |
| | $H_2O$/Mg (des) | 2.16 | 4.08 [a] | | | | 2.02 | 3.37 [a] | |
| | OH/Mg (structural) [b] | 0.80 | | | | | 1.23 | | |
| TGA | $H_2O$/Mg | 1.76 | 2.71 | | 1.84 | 1.83 | 1.83 | 2.60 | |
| | OH/Mg (structural) [c] | 1.43 | 1.46 | | 1.52 | 1.54 | 1.57 | 1.54 | |
| H NMR | bulk water/Mg | --- | 0.08 | | | | --- | 0.04 | |
| | Confined water/Mg | | 1.76 | | | | | 1.46 | |
| | Very confined water/Mg | | 0.26 | | | | | 0.28 | |
| | OH/Mg (structural) | | 1.24 | | | | | 1.64 | |
| CEC | $Mg^{2+}$/Mg | 0.025 | | | 0.025 | 0.025 | 0.025 | | |

*[a] From the DVS measurements of the M-S-H equilibrated at 33% RH; [b] two times the $H_2O$/Si quantified in the sample at <2.5 RH%; [c] structural water plus possibly adsorbed water.*

## 6. References


[1] F. Zhang, Magnesium oxide based binders as low-carbon cements, PhD Thesis, Imperial College London, 2012.

[2] L. Vandeperre, M. Liska, A. Al-Tabbaa, Hydration and mechanical properties of magnesia, pulverized fuel ash, and portland cement blends, Journal of materials in civil engineering, 20 (2008) 375-383.

[3] E. Gartner, M. Gimenez, V. Meyer, A. Pisch, A Novel Atmospheric Pressure Approach to the Mineral Capture of $CO_2$ from Industrial Point Sources, Thirteenth annual conference on carbon capture, utilization and storage, Pittsburgh, Pennsylvania, (2014).

[4] A. Jenni, U. Mäder, C. Lerouge, S. Gaboreau, B. Schwyn, In situ interaction between different concretes and Opalinus clay, Physics and Chemistry of the Earth, Parts A/B/C, 70 (2014) 71-83.
[5] A. Dauzères, G. Achiedo, D. Nied, E. Bernard, S. Alahrache, B. Lothenbach, Magnesium perturbation in low-pH concretes placed in clayey environment - solid characterizations and modeling, Cement and Concrete Research, 79 (2016) 137-150.
[6] J.L. Garcia Calvo, A. Hidalgo, C. Alonso, L. Fernández Luco, Development of low-pH cementitious materials for HLRW repositories: Resistance against ground waters aggression, Cement and Concrete Research, 40 (2010) 1290-1297.
[7] C. Lerouge, S. Gaboreau, S. Grangeon, F. Claret, F. Warmont, A. Jenni, V. Cloet, U. Mäder, In situ interactions between Opalinus Clay and Low Alkali Concrete, Physics and Chemistry of the Earth, Parts A/B/C, 99 (2017) 3-21.
[8] U. Mäder, A. Jenni, C. Lerouge, S. Gaboreau, S. Miyoshi, Y. Kimura, V. Cloet, M. Fukaya, F. Claret, T. Otake, M. Shibata, B. Lothenbach, 5-year chemico-physical evolution of concrete-claystone interfaces, Swiss Journal of Geosciences, 110 (2017) 307-327.
[9] D. Bonen, M.D. Cohen, Magnesium sulfate attack on portland cement paste—II. Chemical and mineralogical analyses, Cement and Concrete Research, 22 (1992) 707-718.
[10] W. Kunther, B. Lothenbach, K.L. Scrivener, Deterioration of mortar bars immersed in magnesium containing sulfate solutions, Materials and structures, 46 (2013) 2003-2011.
[11] K. De Weerdt, H. Justnes, The effect of sea water on the phase assemblage of hydrated cement paste, Cement and Concrete Composites, 55 (2015) 215-222.
[12] E. Bernard, A. Dauzères, B. Lothenbach, Magnesium and calcium silicate hydrates, Part II: Mg-exchange at the interface “low-pH” cement and magnesium environment studied in a C-S-H and M-S-H model system, Applied Geochemistry, 89 (2018) 210-218.
[13] E. Bernard, B. Lothenbach, C. Cau-Dit-Coumes, C. Chlique, A. Dauzères, I. Pochard, Magnesium and calcium silicate hydrates, Part I: Investigation of the possible magnesium incorporation in calcium silicate hydrate (C-S-H) and of the calcium in magnesium silicate hydrate (M-S-H), Applied Geochemistry, 89 (2018) 229-242.
[14] D.R.M. Brew, F.P. Glasser, Synthesis and characterisation of magnesium silicate hydrate gels, Cement and Concrete Research, 35 (2005) 85-98.
[15] D. Nied, K. Enemark-Rasmussen, E. L'Hopital, J. Skibsted, B. Lothenbach, Properties of magnesium silicate hydrates (MSH), Cement and Concrete Research, 79 (2016) 323-332.
[16] C. Roosz, S. Grangeon, P. Blanc, V. Montouillout, B. Lothenbach, P. Henocq, E. Giffaut, P. Vieillard, S. Gaboreau, Crystal structure of magnesium silicate hydrates (MSH): The relation with 2: 1 Mg–Si phyllosilicates, Cement and Concrete Research, 73 (2015) 228-237.
[17] S.A. Walling, H. Kinoshita, S.A. Bernal, N.C. Collier, J.L. Provis, Structure and properties of binder gels formed in the system $Mg(OH)_2$-$SiO_2$-$H_2O$ for immobilisation of Magnox sludge, Dalton Transactions, 44 (2015) 8126-8137.
[18] F. Jin, A. Al-Tabbaa, Thermogravimetric study on the hydration of reactive magnesia and silica mixture at room temperature, Thermochimica Acta, 566 (2013) 162-168.
[19] Z. Li, T. Zhang, J. Hu, Y. Tang, Y. Niu, J. Wei, Q. Yu, Characterization of reaction products and reaction process of $MgO–SiO_2–H_2O$ system at room temperature, Construction and Building Materials, 61 (2014) 252.
[20] J. Szczerba, R. Prorok, E. Śnieżek, D. Madej, K. Maślona, Influence of time and temperature on ageing and phases synthesis in the $MgO–SiO_2–H_2O$ system, Thermochimica Acta, 567 (2013) 57-64.

[21] T. Zhang, C. Cheeseman, L. Vandeperre, Development of low pH cement systems forming magnesium silicate hydrate (MSH), Cement and Concrete Research, 41 (2011) 439-442.
[22] E. Bernard, B. Lothenbach, D. Rentsch, I. Pochard, A. Dauzères, Formation of magnesium silicate hydrates (M-S-H), Physics and Chemistry of the Earth, Parts A/B/C, 99 (2017) 142-157.
[23] A. Pedone, F. Palazzetti, V. Barone, Models of Aged Magnesium–Silicate–Hydrate Cements Based on the Lizardite and Talc Crystals: A Periodic DFT-GIPAW Investigation, The Journal of Physical Chemistry C, (2017).
[24] M. Sánchez del Río, E. García-Romero, M. Suárez, I.d. Silva, L. Fuentes-Montero, G. Martínez-Criado, Variability in sepiolite: Diffraction studies, American Mineralogist, 96 (2011) 1443-1454.
[25] J.W. Gruner, The crystal structures of talc and pyrophyllite, Zeitschrift für Kristallographie-Crystalline Materials, 88 (1934) 412-419.
[26] F. Zigan, R. Rothbauer, Neutron diffraction measurement on brucite, Neues Jahrb Mineral, Monatsh, 4 (1967) 137-143.
[27] M. Mellini, P.F. Zanazzi, Crystal structures of lizardite-1T and lizardite-2H1 from Coli, Italy, American Mineralogist, 72 (1987) 943-948.
[28] I. Dódony, M. Pósfai, P.R. Buseck, Revised structure models for antigorite: An HRTEM study, American Mineralogist, 87 (2002) 1443-1457.
[29] K. Momma, F. Izumi, VESTA 3 for three-dimensional visualization of crystal, volumetric and morphology data, Journal of Applied Crystallography, 44 (2011) 1272-1276.
[30] M. Tonelli, F. Martini, L. Calucci, E. Fratini, M. Geppi, F. Ridi, S. Borsacchi, P. Baglioni, Structural characterization of magnesium silicate hydrate: towards the design of eco-sustainable cements, Dalton Transactions, 45 (2016) 3294-3304.
[31] K.J.D. MacKenzie, R.H. Meinhold, Thermal reaction of chrysotile revisited: a $^{29}$Si and $^{25}$Mg NMR study, American Mineralogist, 79 (1994) 43-50.
[32] B. Rhouta, H. Kaddami, J. Elbarqy, M. Amjoud, L. Daoudi, F. Maury, F. Senocq, A. Maazouz, J.-F. Gerard, Elucidating the crystal-chemistry of Jbel Rhassoul stevensite (Morocco) by advanced analytical techniques, Clay minerals, 43 (2008) 393-403.
[33] K. Chabrol, M. Gressier, N. Pebere, M.-J. Menu, F. Martin, J.-P. Bonino, C. Marichal, J. Brendle, Functionalization of synthetic talc-like phyllosilicates by alkoxyorganosilane grafting, Journal of Materials Chemistry, 20 (2010) 9695-9706.
[34] A. Dumas, F. Martin, C. Le Roux, P. Micoud, S. Petit, E. Ferrage, J. Brendlé, O. Grauby, M. Greenhill-Hooper, Phyllosilicates synthesis: a way of accessing edges contributions in NMR and FTIR spectroscopies. Example of synthetic talc, Physics and Chemistry of Minerals, 40 (2013) 361-373.
[35] E. Bernard, Magnesium silicate hydrate (M-S-H and M-A-S-H) characterization in temperature, calcium, and alkali conditions, Université Bourgogne Franche Comté, 2017.
[36] P.F. Barron, P. Slade, R.L. Frost, Solid-state silicon-29 spin-lattice relaxation in several 2: 1 phyllosilicate minerals, The Journal of Physical Chemistry, 89 (1985) 3305-3310.
[37] M.R. Weir, W. Kuang, G.A. Facey, C. Detellier, Solid-state nuclear magnetic resonance study of sepiolite and partially dehydrated sepiolite, Clays and Clay Minerals, 50 (2002) 240-247.
[38] M. Aramendía, V. Borau, C. Jiménez, J. Marinas, J. Ruiz, Characterization of Spanish sepiolites by high-resolution solid-state NMR, Solid state nuclear magnetic resonance, 8 (1997) 251-256.
[39] J.-B. d'Espinose de la caillerie, J. Fripiat, A reassessment of the $^{29}$Si MAS-NMR spectra of sepiolite and aluminated sepiolite, Clay minerals, 29 (1994) 313-318.

[40] R. Wollast, F.T. MacKenzie, O.P. Bricker, Experimental precipitation and genesis of sepiolite at earth-surface conditions, The American Mineralogist, 53 (1968) 1645-1662.
[41] H. Nagata, S. Shimoda, T. Sudo, On dehydration f bound water of sepiolite, Clays & Clay Minerals, Citeseer, 1974.
[42] R.L. Frost, Z. Ding, Controlled rate thermal analysis and differential scanning calorimetry of sepiolites and palygorskites, Thermochimica Acta, 397 (2003) 119-128.
[43] W.-S. Chiang, G. Ferraro, E. Fratini, F. Ridi, Y.-Q. Yeh, U. Jeng, S.-H. Chen, P. Baglioni, Multiscale structure of calcium-and magnesium-silicate-hydrate gels, Journal of Materials Chemistry A, 2 (2014) 12991-12998.
[44] E. L'Hôpital, B. Lothenbach, G. Le Saout, D. Kulik, K. Scrivener, Incorporation of aluminium in calcium-silicate-hydrates, Cement and Concrete Research, 75 (2015) 91-103.
[45] D. Massiot, F. Fayon, M. Capron, I. King, S. Le Calvé, B. Alonso, J.O. Durand, B. Bujoli, Z. Gan, G. Hoatson, Modelling one-and two-dimensional solid-state NMR spectra, Magnetic Resonance in Chemistry, 40 (2002) 70-76.
[46] J.-B. d'Espinose de Lacaillerie, M. Kermarec, O. Clause, $^{29}$Si NMR observation of an amorphous magnesium silicate formed during impregnation of silica with Mg(II) in aqueous solution, The Journal of Physical Chemistry, 99(47) (1995) 17273-17281.
[47] C. Meral, C. Benmore, P.J. Monteiro, The study of disorder and nanocrystallinity in C–S–H, supplementary cementitious materials and geopolymers using pair distribution function analysis, Cement and Concrete Research, 41 (2011) 696-710.
[48] C.E. White, J.L. Provis, B. Bloomer, N.J. Henson, K. Page, In situ X-ray pair distribution function analysis of geopolymer gel nanostructure formation kinetics, Physical Chemistry Chemical Physics, 15 (2013) 8573-8582.
[49] T. Egami, S.J.L. Billinge, Chapter 3. The method of total scattering and atomic pair distribution function analysis, Pergamon Materials Series2003.
[50] X. Qiu, J.W. Thompson, S.J. Billinge, PDFgetX2: a GUI-driven program to obtain the pair distribution function from X-ray powder diffraction data, Journal of Applied Crystallography, 37 (2004) 678-678.
[51] C. Farrow, P. Juhas, J. Liu, D. Bryndin, E. Božin, J. Bloch, T. Proffen, S. Billinge, PDFfit2 and PDFgui: computer programs for studying nanostructure in crystals, Journal of Physics: Condensed Matter, 19 (2007) 335219.
[52] S. Brunauer, P.H. Emmett, E. Teller, Adsorption of gases in multimolecular layers, Journal of the American chemical society, 60 (1938) 309-319.
[53] B.C. Lippens, J. De Boer, Studies on pore systems in catalysts: V. The t method, Journal of Catalysis, 4 (1965) 319-323.
[54] K. Sing, D. Everett, R. Haul, L. Moscou, R. Pierotti, J. Rouquerol, T. Siemieniewska, Reporting physisorption data for gas/solid systems with special reference to the determination of surface area and porosity, Pure and Applied Chemistry, 57 (1985) 603-619.
[55] D. Everett, Manual of symbols and terminology for physicochemical quantities and units, appendix II: Definitions, terminology and symbols in colloid and surface chemistry, Pure and Applied Chemistry, 31 (1972) 577-638.
[56] M. Wyrzykowski, P.J. McDonald, K.L. Scrivener, P. Lura, Water Redistribution within the Microstructure of Cementitious Materials due to Temperature Changes Studied with 1H NMR, The Journal of Physical Chemistry C, 121 (2017) 27950-27962.
[57] A.C.A. Muller, J. Mitchell, P.J. McDonald, Proton nuclear magnetic resonance relaxometry, in: K. Scrivener, R. Snellings, B. Lothenbach (Eds.) A Practical Guide to Microstructural Analysis of Cementitious Materials, CRC Press, Oxford, UK, 2016, pp. 177-212.

[58] A. Valori, P.J. McDonald, K.L. Scrivener, The morphology of C–S–H: Lessons from 1 H nuclear magnetic resonance relaxometry, Cement and Concrete Research, 49 (2013) 65-81.
[59] M. Fleury, E. Kohler, F. Norrant, S. Gautier, J. M'Hamdi, L. Barré, Characterization and quantification of water in smectites with low-field NMR, The Journal of Physical Chemistry C, 117 (2013) 4551-4560.
[60] F. D'Orazio, S. Bhattacharja, W.P. Halperin, K. Eguchi, T. Mizusaki, Molecular diffusion and nuclear-magnetic-resonance relaxation of water in unsaturated porous silica glass, Physical Review B, 42 (1990) 9810.
[61] M. James, R.J. Hunter, R.W. O'Brien, Effect of particle size distribution and aggregation on electroacoustic measurements of. zeta. potential, Langmuir, 8 (1992) 420-423.
[62] T. Mitsuda, H. Taguchi, Formation of magnesium silicate hydrate and its crystallzation to talc, Cement and Concrete Research, 7 (1977) 223-230.
[63] J.C.S. Yang, The system magnesia-silica-water below 300° C.: I, Low-temperature phases from 100° to 300° C. and their properties, Journal of the American Ceramic Society, 43 (1960) 542-549.
[64] G. Brindley, D. Bish, H.-M. Wan, Compositions, structures, and properties of nickel-containing minerals in the kerolite-pimelite series, American Mineralogist, 64 (1979) 615-625.
[65] G. Brindley, D.L. Bistt, H.-m. Wan, The nature of kerolite, its relation to talc and stevensite, (1977).
[66] D.L. Bish, G. Brindley, Deweylites, mixtures of poorly crystalline hydrous serpentine and talc-like minerals, Mineral. Mag, 42 (1978) 75-79.
[67] L. Lin, D. Cornu, M.M. Daou, C. Domingos, V. Herledan, J.-M. Krafft, G. Laugel, Y. Millot, H. Lauron-Pernot, Role of Water on the Activity of Magnesium Silicate for Transesterification Reactions, ChemCatChem, Wiley Omline Library, 9 (2017).
[68] G. Falini, E. Foresti, M. Gazzano, A.F. Gualtieri, M. Leoni, I.G. Lesci, N. Roveri, Tubular-Shaped Stoichiometric Chrysotile Nanocrystals, Chemistry-A European Journal, 10 (2004) 3043-3049.
[69] R. Vogels, J.T. Kloprogge, J.W. Geus, Synthesis and characterization of saponite clays, American Mineralogist, 90 (2005) 931-944.
[70] C. Bisio, G. Gatti, E. Boccaleri, L. Marchese, G. Superti, H. Pastore, M. Thommes, Understanding physico–chemical properties of saponite synthetic clays, Microporous and Mesoporous Materials, 107 (2008) 90-101.
[71] L. Michot, F. Villieras, M. François, J. Yvon, R. Le Dred, J. Cases, The structural microscopic hydrophilicity of talc, Langmuir, 10 (1994) 3765-3773.
[72] S. Chevalier, R. Franck, J. Lambert, D. Barthomeuf, H. Suquet, Characterization of the porous structure and cracking activity of Al-pillared saponites, Applied Catalysis A: General, 110 (1994) 153-165.
[73] R.L. Frost, J.T. Kloprogge, Infrared emission spectroscopic study of brucite, Spectrochimica Acta Part A: Molecular and Biomolecular Spectroscopy, 55 (1999) 2195-2205.
[74] R.L. Frost, O.B. Locos, H. Ruan, J.T. Kloprogge, Near-infrared and mid-infrared spectroscopic study of sepiolites and palygorskites, Vibrational Spectroscopy, 27 (2001) 1-13.
[75] M.L. Hair, Hydroxyl groups on silica surface, Journal of Non-Crystalline Solids, 19 (1975) 299-309.
[76] R.L. Frost, E. Mendelovici, Modification of fibrous silicates surfaces with organic derivatives: an infrared spectroscopic study, Journal of colloid and interface science, 294 (2006) 47-52.

[77] C. Roosz, S. Gaboreau, S. Grangeon, D. Prêt, V. Montouillout, N. Maubec, S. Ory, P. Blanc, P. Vieillard, P. Henocq, Distribution of water in synthetic calcium silicate hydrates, Langmuir, 32 (2016) 6794-6805.
[78] J. Cases, I. Bérend, G. Besson, M. Francois, J. Uriot, F. Thomas, J. Poirier, Mechanism of adsorption and desorption of water vapor by homoionic montmorillonite. 1. The sodium-exchanged form, Langmuir, 8 (1992) 2730-2739.
[79] L. Zhuravlev, The surface chemistry of amorphous silica. Zhuravlev model, Colloids and Surfaces A: Physicochemical and Engineering Aspects, 173 (2000) 1-38.
[80] E. L'Hôpital, B. Lothenbach, D. Kulik, K. Scrivener, Influence of calcium to silica ratio on aluminium uptake in calcium silicate hydrate, Cement and Concrete Research, 85 (2016) 111-121.
[81] V. Ivanova, B. Kasatov, V. Moskaleva, Thermographic studies of serpentines by ignition up to 1400° C, International Geology Review, 16 (1974) 202-213.
[82] J.D. Miller, J. Nalaskowski, B. Abdul, H. Du, Surface characteristics of kaolinite and other selected two layer silicate minerals, The Canadian Journal of Chemical Engineering, 85 (2007) 617-624.
[83] O.S. Pokrovsky, J. Schott, Experimental study of brucite dissolution and precipitation in aqueous solutions: surface speciation and chemical affinity control, Geochimica et Cosmochimica Acta, 68 (2004) 31-45.
[84] J.R.F. Giese, W. Wu, C.J. Van Oss, Surface and electrokinetic properties of clays and other mineral particles, untreated and treated with organic or inorganic cations, Journal of dispersion science and technology, 17 (1996) 527-547.
[85] L.S. de Lara, V.A. Rigo, M.F. Michelon, C.O. Metin, Q.P. Nguyen, C.R. Miranda, Molecular dynamics studies of aqueous silica nanoparticle dispersions: salt effects on the double layer formation, Journal of Physics: Condensed Matter, 27 (2015) 325101.
[86] M.C. Bruzzoniti, R.M. De Carlo, S. Fiorilli, B. Onida, C. Sarzanini, Functionalized SBA-15 mesoporous silica in ion chromatography of alkali, alkaline earths, ammonium and transition metal ions, Journal of Chromatography A, 1216 (2009) 5540-5547.
[87] J.M. Skluzacek, M.I. Tejedor, M.A. Anderson, An iron-modified silica nanofiltration membrane: Effect of solution composition on salt rejection, Microporous and mesoporous materials, 94 (2006) 288-294.
[88] H. Shariatmadari, A. Mermut, M. Benke, Sorption of selected cationic and neutral organic molecules on palygorskite and sepiolite, Clays and Clay Minerals, 47 (1999) 44-53.
[89] H. Gailhanou, P. Blanc, J. Rogez, G. Mikaelian, K. Horiuchi, Y. Yamamura, K. Saito, H. Kawaji, F. Warmont, J.-M. Grenèche, Thermodynamic properties of saponite, nontronite, and vermiculite derived from calorimetric measurements, American Mineralogist, 98 (2013) 1834-1847.
[90] D. Costenaro, G. Gatti, F. Carniato, G. Paul, C. Bisio, L. Marchese, The effect of synthesis gel dilution on the physico-chemical properties of acid saponite clays, Microporous and Mesoporous Materials, 162 (2012) 159-167.
[91] A. Kaya, Y. Yukselen, Zeta potential of clay minerals and quartz contaminated by heavy metals, Canadian Geotechnical Journal, 42 (2005) 1280-1289.
[92] G.D. Markham, J.P. Glusker, C.W. Bock, The arrangement of first-and second-sphere water molecules in divalent magnesium complexes: Results from molecular orbital and density functional theory and from structural crystallography, The Journal of Physical Chemistry B, 106 (2002) 5118-5134.